DISEASES AND DISORDERS

KAT6A deficiency impairs cognitive functions through suppressing RSPO2/Wnt signaling in hippocampal CA3

Yongqing Liu[1], Minghua Fan[2], Junhua Yang[1], Ljubica Mihaljević[1], Kevin Hong Chen[1], Yingzhi Ye[1], Shuying Sun[1,2], Zhaozhu Qiu[1,2,3]*

Intellectual disability (ID) affects ~2% of the population and ID-associated genes are enriched for epigenetic factors, including those encoding the largest family of histone lysine acetyltransferases (KAT5-KAT8). Among them is *KAT6A*, whose mutations cause KAT6A syndrome, with ID as a common clinical feature. However, the underlying molecular mechanism remains unknown. Here, we find that KAT6A deficiency impairs synaptic structure and plasticity in hippocampal CA3, but not in CA1 region, resulting in memory deficits in mice. We further identify a CA3-enriched gene *Rspo2*, encoding Wnt activator R-spondin 2, as a key transcriptional target of KAT6A. Deletion of *Rspo2* in excitatory neurons impairs memory formation, and restoring RSPO2 expression in CA3 neurons rescues the deficits in Wnt signaling and learning-associated behaviors in *Kat6a* mutant mice. Collectively, our results demonstrate that KAT6A-RSPO2-Wnt signaling plays a critical role in regulating hippocampal CA3 synaptic plasticity and cognitive function, providing potential therapeutic targets for KAT6A syndrome and related neurodevelopmental diseases.

INTRODUCTION

The development of central nervous system and the learning-induced rewiring of neural circuits are tightly modulated through the dynamic regulation of gene expression (*1*, *2*). Acetylation of histones is a key mechanism regulating chromatin organization and gene expression (*3*). While histone deacetyltransferases have been the focus of intense research, the role of histone acetyltransferases (HATs) in the brain is underexplored. The five-member MYST proteins represent the largest family of HATs in humans, whose gene mutations often cause neurodevelopmental diseases characterized with intellectual disability (ID) (*4*–*8*).

One of MYST family member lysine acetyltransferase 6A (KAT6A) [also known as monocytic leukemia zinc finger (MOZ) and MYST3] was first identified as an oncogene rearranged in acute myeloid leukemia (*9*). It is composed of a double plant homeodomain finger that binds to acetylated histone tails, the HAT domain, and a long unstructured C-terminal region. KAT6A plays an important role in tumor growth, body segment patterning, and hematopoietic stem cell maintenance (*10*–*12*). Heterozygous nonsense (protein-truncating, most likely loss-of-function) mutations of *KAT6A* also cause a rare genetic disorder KAT6A syndrome (or Arboleda-Tham syndrome), with ~400 patients reported so far around the world (*13*). With the increased application of whole-exome sequencing, the number of diagnosed individuals will likely grow much larger. KAT6A syndrome is characterized by several common clinical traits including ID, speech and language deficits, and global developmental delay, along with less penetrant phenotypes such as microcephaly, neonatal hypotonia, and autism spectrum disorder (*13*). Most of the pathogenic variants for KAT6A syndrome are protein-truncating mutations that occur throughout the gene. However, patients with mutations in last two exons (exons 16 and 17) have more severe ID and other phenotypes, compared to those with early truncating mutations (*13*). It is possible that these late-truncating mutations are not subjected to nonsense-mediated mRNA decay. The resulting truncated KAT6A proteins may have dominant negative effects. Nevertheless, the impact of *KAT6A* loss of function in the nervous system and the underlying mechanism, leading to the brain disease remain elusive. Here, we uncover a KAT6A/RSPO2/Wnt signaling cascade that is required for learning and memory by regulating synaptic structure and plasticity in hippocampal CA3 pyramidal neurons and provide new insights into our understanding of the pathogenesis of KAT6A syndrome.

RESULTS

Kat6a haploinsufficiency results in cognitive deficits in mice

To elucidate the mechanism behind KAT6A syndrome and assess the effect of KAT6A deletion in the brain, we first generated *Kat6a*-floxed mice using the efficient additions with single-strand DNA (ssDNA) inserts–CRISPR (*Easi*-CRISPR) method (*14*) (Fig. 1A and fig. S1A). During the insertion of a floxed cassette, we also obtained *Kat6a* knockout allele because of deletion of the target exon (Fig. 1A and fig. S1, B and C). *Kat6a* homozygous knockout mice were embryonic lethal (*12*); hence, we tested haploinsufficiency in $Kat6a^{+/-}$ mice with exon 4 deletion that results in a premature stop codon. Therefore, it probably mimics patients with early truncating mutations. The mRNA level of *Kat6a* in hippocampus of $Kat6a^{+/-}$ mice was ~50% of that in wild-type (WT) littermates (Fig. 1B). Both male and female $Kat6a^{+/-}$ mice displayed smaller body weight than WT littermates starting at weaning age and throughout adulthood (Fig. 1C and fig. S1, D and E), consistent with growth delays of patients with KAT6A syndrome.

We then performed a battery of behavioral assays to compare the performance of $Kat6a^{+/-}$ and their WT littermates in adulthood. In the open-field test, $Kat6a^{+/-}$ mice showed more time spent at the center of the chamber compared to control mice, whereas both groups showed comparable total distance traveled (fig. S1F), indicating that the mutant mice have normal locomotor activity but with less anxiety levels. The reduced anxiety was further confirmed by the elevated plus maze test (fig. S1G). In addition, we used the three-chamber assay to

[1]Department of Physiology, Johns Hopkins University School of Medicine, Baltimore, MD 21205, USA. [2]Solomon H. Snyder Department of Neuroscience, Johns Hopkins University School of Medicine, Baltimore, MD 21205, USA. [3]Department of Neurosurgery, Johns Hopkins University School of Medicine, Baltimore, MD 21205, USA. *Corresponding author. Email: zhaozhu@jhmi.edu

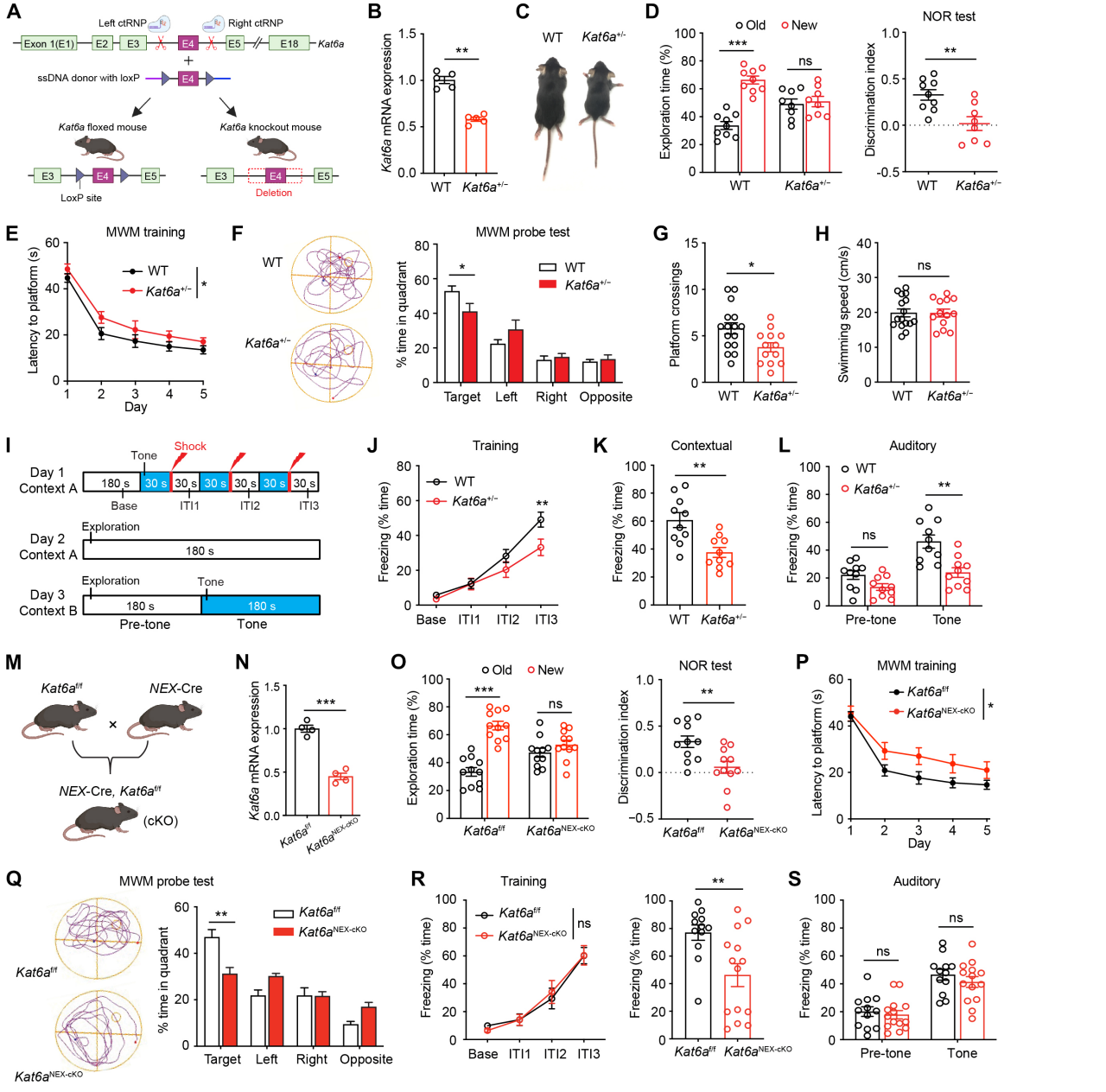

Fig. 1. KAT6A deficiency impairs learning and memory in mice. (**A**) Schematic diagram. (**B**) qRT-PCR analysis of total hippocampal mRNA from WT and *Kat6a*$^{+/-}$ mice. $n = 5$ mice per group. (**C**) Representative images of body size of 4-week-old WT and *Kat6a*$^{+/-}$ mice. (**D**) The NOR test. $n = 8$ to 9 mice per group. (**E**) Time spent before reaching the hidden platform during training days in the MWM test. Two-way ANOVA test. $F(1, 27) = 5.645$, $^*P = 0.025$. $n = 13$ to 16 mice per group. (**F**) Representative traces and time spent in different quadrants during the probe test. (**G** and **H**) Entries into platform zone and swimming speed in the MWM test. Unpaired Student's *t* test. (**I**) Schematic diagram of fear conditioning test. ITI, intertrial interval. (**J**) Learning curves during the training sessions in fear conditioning test. Two-way ANOVA test. $n = 10$ mice per group. (**K**) Contextual test. Unpaired Student's *t* test. (**L**) Auditory test. Two-way ANOVA test. (**M**) *Kat6a*$^{f/f}$ mice crossed with *NEX*-cre mice to obtain the *Kat6a*$^{NEX\text{-}cKO}$ mice. (**N**) qRT-PCR analysis of total hippocampal mRNA from *Kat6a*$^{f/f}$ and *Kat6a*$^{NEX\text{-}cKO}$ mice. $n = 4$ mice per group. (**O**) The NOR test. $n = 11$ mice per group. (**P**) Time spent before reaching the hidden platform during training days in the MWM test. Two-way ANOVA test. $F(1, 20) = 6.713$, $^*P = 0.017$. (**Q**) The probe test of the MWM test. $n = 11$ mice per group. (**R**) Left: Learning curves during the training sessions in fear conditioning test. Two-way ANOVA test. $F(1, 24) = 0.004$, $P = 0.952$. Right: Contextual test. $n = 12$ *Kat6a*$^{f/f}$ and $n = 14$ *Kat6a*$^{NEX\text{-}cKO}$ mice. Unpaired Student's *t* test. (**S**) Auditory test. $^*P < 0.05$, $^{**}P < 0.01$, and $^{***}P < 0.001$. ns, nonsignificant. Data are presented as mean ± SEM.

examine the sociability of WT and *Kat6a*$^{+/-}$ mice. When compared with WT mice, the majority of *Kat6a*$^{+/-}$ mice exhibited normal social ability (fig. S1, H and I), consistent with the notion that many parents describe their children with KAT6A mutations as happy and sociable despite ID and developmental delays.

Considering that ID is a prominent clinical feature of KAT6A syndrome, we further investigated whether KAT6A loss affects cognitive functions in mice. In the novel object recognition (NOR) test, which evaluates the preference of mice to explore a new object over a familiar object, WT littermates displayed a significant preference for the novel object (Fig. 1D). However, *Kat6a*$^{+/-}$ mice showed no such preference (Fig. 1D), indicating a deficit in recognition memory.

To test hippocampus-dependent spatial learning and memory, we used the Morris water maze (MWM) assay to test an animal's ability to use spatial cues to locate a hidden platform in a tank of water. During the training sessions, *Kat6a*$^{+/-}$ mice spent a longer time navigating to the platform than control mice (Fig. 1E), indicating that their spatial learning is impaired. In the probe test, *Kat6a*$^{+/-}$ mice spent less time in the target quadrant (Fig. 1, F and G), whereas their swimming activity was normal (Fig. 1H), suggesting that spatial memory is impaired in the mutant mice.

To further confirm the importance of KAT6A in learning and memory, we performed a classic fear conditioning procedure, in which we paired an auditory cue with a mild aversive foot shock (Fig. 1I). Contextual fear memory is sensitive to hippocampal defects, whereas auditory fear memory depends on amygdala function (*15*). During the training sessions, *Kat6a*$^{+/-}$ mice exhibited decreased foot shock–evoked freezing behavior compared with WT controls (Fig. 1J), suggesting that their learning ability is impaired. At 24 hours after conditioning, mice were placed back into the training context and their freezing time was measured. Compared with controls, *Kat6a*$^{+/-}$ mice displayed significantly decreased context-evoked freezing behaviors (Fig. 1K). Likewise, decreased tone-evoked freezing behaviors were also observed in the mutants (Fig. 1L). Together, these data demonstrate that *Kat6a* haploinsufficiency results in memory deficits in mice.

Excitatory neuron–specific deletion of KAT6A is sufficient to cause memory deficits

In the central nervous system, KAT6A is ubiquitously expressed across different cell types. To explore which cell type in the brain is susceptible to the loss of KAT6A function in the context of cognitive defects, we first crossed *Kat6a* floxed mice (*Kat6a*$^{f/f}$) with *NEX*-cre mice that express Cre recombinase in pyramidal neurons in the neocortex and hippocampus (*Kat6a*$^{NEX\text{-}cKO}$) (Fig. 1M). In the *Kat6a*$^{NEX\text{-}cKO}$ mice, the level of *Kat6a* mRNA was significantly reduced in hippocampus (Fig. 1N). Notably, compared to control littermates, adult *Kat6a*$^{NEX\text{-}cKO}$ mice appeared grossly normal, with normal cortical morphology (fig. S2, A to C), hippocampal cell density (fig. S2D), body weight (fig. S2E), and adult hippocampal neurogenesis (fig. S2F). However, similar to *Kat6a*$^{+/-}$, *Kat6a*$^{NEX\text{-}cKO}$ mice also displayed reduced anxiety levels (fig. S2, G to H). Moreover, *Kat6a*$^{NEX\text{-}cKO}$ mice exhibited memory deficits in the NOR test and the MWM test (Fig. 1, O to Q), suggesting that mice with KAT6A deletion in excitatory neurons recapitulate the memory deficits in *Kat6a*$^{+/-}$ mice. In the fear conditioning test, compared with control mice, both male (Fig. 1R) and female (fig. S2I) *Kat6a*$^{NEX\text{-}cKO}$ mice displayed significantly decreased context-evoked freezing behavior, whereas there was no difference in baseline freezing in a new context and no difference in elevated freezing due to the tone presentation (Fig. 1S and fig. S2I), indicating that memory deficits of *Kat6a*$^{NEX\text{-}cKO}$ mice are specific to hippocampus-dependent contextual fear conditioning.

To bypass any potential developmental effects and further validate that excitatory neuronal loss of KAT6A leads to cognitive deficits, we carried out a second cross with the *Camk2a*-cre mice (fig. S3A), where Cre expression starts at 2 to 3 weeks after birth and is restricted to forebrain excitatory neurons in hippocampus and cortex. Similar to *Kat6a*$^{NEX\text{-}cKO}$, *Kat6a*$^{Camk2a\text{-}cKO}$ mice also displayed memory defects in the learning-related behaviors (fig. S3), while showing normal locomotion, anxiety level, and sociability (fig. S3). In contrast, ablation of KAT6A in astrocytes by *Gfap*-cre (fig. S4, A to E) or in inhibitory neurons by *Gad2*-cre (fig. S4F) did not induce cognitive dysfunction. Together, these results demonstrate that loss of KAT6A specifically in excitatory neurons is sufficient to cause memory deficits in mice.

KAT6A deficiency impairs hippocampal CA3 synaptic plasticity

To investigate whether deletion of KAT6A influences neuronal function in mouse hippocampus, a pivotal region implicated in learning and memory, we performed whole-cell patch-clamp recordings on acute hippocampal slices to first examine the basal synaptic transmission of CA1 pyramidal neurons (Fig. 2A). Unexpectedly, miniature excitatory postsynaptic currents (mEPSCs) of CA1 pyramidal neurons were comparable in frequency and amplitude between *Kat6a*$^{NEX\text{-}cKO}$ mice and control littermates (Fig. 2B). In addition, both paired-pulse ratios (Fig. 2C) and long-term potentiation (LTP) (Fig. 2D) in dorsal CA1 region were normal in *Kat6a*$^{NEX\text{-}cKO}$ mice, suggesting that KAT6A deficiency has no obvious effect on CA1 neuronal function.

Given that the hippocampal CA3 region is also implicated in memory function (*16*–*18*), we next measured mEPSC in CA3 pyramidal neurons. mEPSC frequency was substantially decreased in *Kat6a*$^{NEX\text{-}cKO}$ mice compared to controls, whereas amplitude was not changed (Fig. 2E), suggesting that KAT6A deficiency causes defects in CA3 glutamatergic synaptic transmission. CA3 pyramidal neurons receive three main types of glutamatergic inputs: Recurrent CA3 collaterals, mossy fiber (MF) inputs from DG granule cells, and perforant path inputs from entorhinal cortex (*18*). To further examine which input contributes to this defect, we recorded mEPSCs while blocking MF inputs and partial perforant path inputs using the group II metabotropic glutamate receptor agonist (2S,2′R,3′R)-2-(2′,3′-Dicarboxycyclopropyl)glycine (DCG-IV) (*19*, *20*). In the presence of DCG-IV, a significant decrease in mEPSC frequency was still observed in CA3 pyramidal neurons of *Kat6a*$^{NEX\text{-}cKO}$ mice (Fig. 2F), indicating that CA3 recurrent synaptic transmission is mainly impaired in the absence of KAT6A.

To explore the underlying mechanisms responsible for the defects in synaptic transmission upon deletion of *Kat6a*, we filled CA3 pyramidal neurons with biocytin and imaged their dendritic branches (Fig. 2G). While the dendrite arbors were not changed in *Kat6a*$^{NEX\text{-}cKO}$ mice by Sholl analysis (Fig. 2H), we observed a significant decrease in spine density at CA3 stratum radiatum, a main region receiving CA3 recurrent inputs (Fig. 2I). Furthermore, in the presence of DCG-IV, LTP induced by high-frequency stimulation at associational and commissural (A/C) fibers to CA3 synapses of the mutant mice was partially but significantly reduced (Fig. 2, J to L). Collectively, the above data suggest that deletion of KAT6A in excitatory neurons impairs hippocampal CA3 synaptic plasticity, thus contributing to the learning and memory deficits.

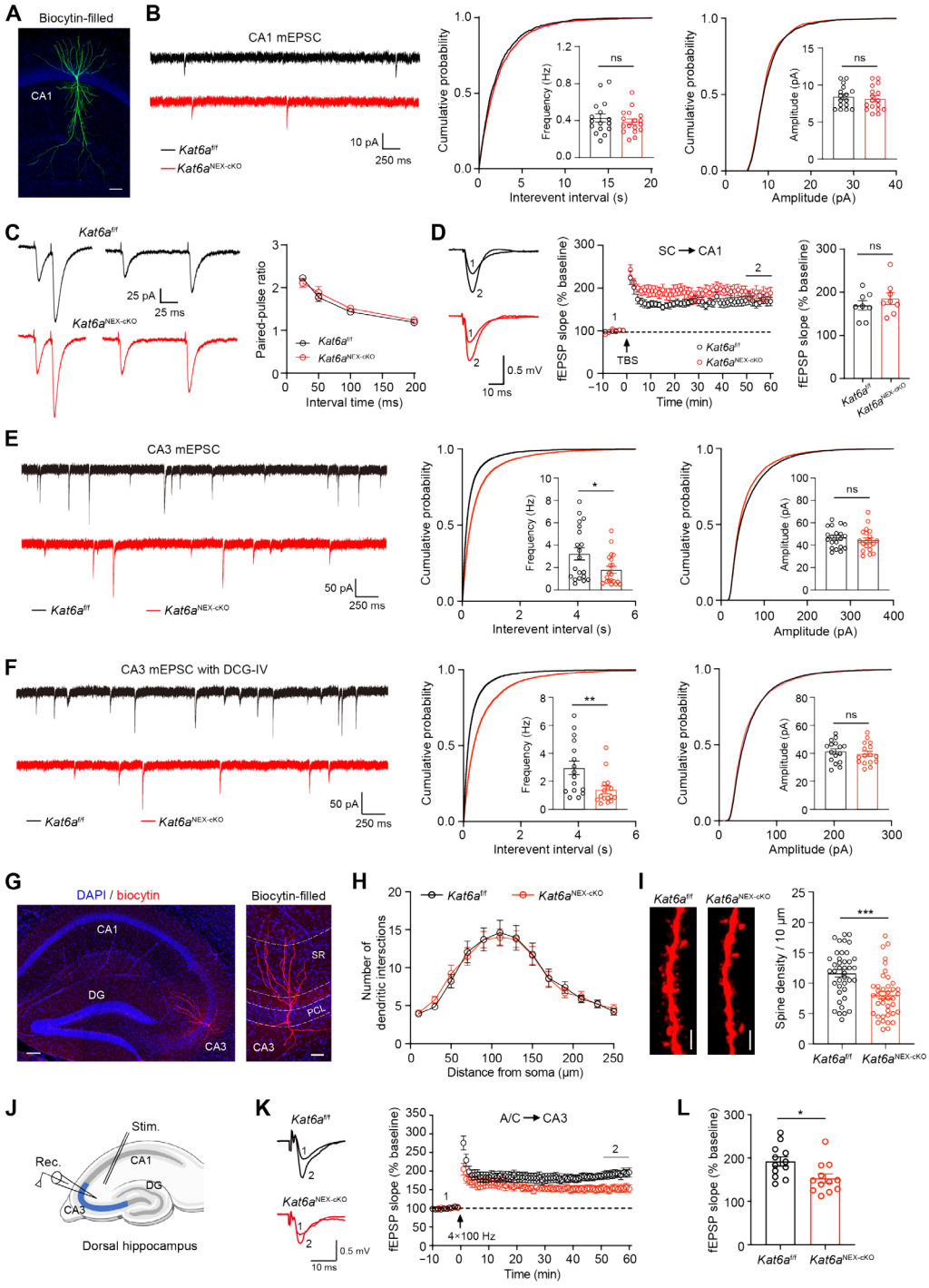

Fig. 2. Loss of KAT6A results in hippocampal CA3 synaptic plasticity defects. (**A**) Representative biocytin-filled CA1 pyramidal neurons from *Kat6a*$^{f/f}$ mice. Scale bar, 50 μm. (**B**) Representative traces (left) and quantification of frequency (middle) and amplitude (right) of mEPSC in dorsal CA1 pyramidal neurons. $n = 16$ to 17 cells from four mice per group. Unpaired Student's *t* test. (**C**) PPRs with different interstimulus intervals. $n = 16$ cells from three mice per group. Two-way ANOVA test. (**D**) TBS-induced LTP at Schaffer collateral (SC) to CA1 synapses. Arrow indicates LTP induction. $n = 8$ slices from four mice per group. Unpaired Student's *t* test. (**E**) mEPSC in dorsal CA3 pyramidal neurons. $n = 20$ cells from four mice per group. Mann-Whitney test. (**F**) mEPSC in the presence of DCG-IV in dorsal CA3 pyramidal neurons. $n = 16$ cells from four mice per group. Mann-Whitney test. (**G**) Left: Representative biocytin-filled CA3 pyramidal neurons from *Kat6a*$^{f/f}$ mice. Scale bar, 100 μm. Right: Different layers in CA3 region. Scale bar, 40 μm. SR, stratum radiatum. PCL, pyramidal cell layer. DAPI, 4′,6-diamidino-2-phenylindole. (**H**) Quantification of CA3 pyramidal neuron dendritic intersections revealed by Sholl analysis. $n = 13$ cells from four mice per group. (**I**) Left: Representative images of dendritic segments in the stratum radiatum dendrites of CA3 pyramidal neurons. Scale bars, 2 μm. Right: Quantification of dendritic spine numbers. $n = 40$ dendrites from four mice per group. Unpaired Student's *t* test. (**J**) Illustration of LTP at CA3 recurrent synapses. (**K**) 4× high-frequency stimulation (HFS)-induced LTP in the presence of DCG-IV at A/C to CA3 synapses. (**L**) The averaged fEPSP slopes during 50 to 60 min after the stimulation. $n = 12$ slices from four mice per group. Unpaired Student's *t* test. $^*P < 0.05$, $^{**}P < 0.01$, and $^{***}P < 0.001$. ns, nonsignificant. Data are presented as mean ± SEM.

snRNA-seq reveals transcriptional targets of KAT6A in hippocampal CA3

To decipher the molecular mechanisms of *Kat6a* haploinsufficiency–induced memory defects, RNA sequencing (RNA-seq) was performed with total RNA extracted from hippocampus of *Kat6a*$^{+/-}$ mice and their WT littermates. A cutoff of *P* value <0.05 and $|\log_2 FC| > 0.2$ was applied to identify differentially expressed genes (Fig. 3A). Because KAT6A mainly acts as a transcriptional coactivator, we focused on gene down-regulation, as these genes are more likely to be its direct targets. A total of 185 genes were down-regulated in hippocampus of *Kat6a*$^{+/-}$ mice (Fig. 3B), which were classified into various signaling pathways using gene ontology (GO) enrichment analysis with a cutoff of *q* value <0.05. Many of the down-regulated genes are involved in the Wnt signaling pathway and excitatory synapse function (Fig. 3C and table S1), supporting the idea that KAT6A plays an important role in developmental processes and regulation of synaptic plasticity.

As cell type–specific changes in the transcriptome can be difficult to detect using bulk RNA-seq in the brain tissues that consist of complex mixtures of cells, we next performed snRNA-seq to more precisely unravel, which genes are changed upon *Kat6a* deletion in excitatory neurons. Hippocampal nuclei from *Kat6a*$^{NEX\text{-}cKO}$ and *Kat6a*$^{f/f}$ mice were isolated and subsequently sorted using the 10x Genomics platform (Fig. 3D). Transcripts were sequenced from 18,421 and 17,806 nuclei from hippocampi of *Kat6a*$^{NEX\text{-}cKO}$ and control mice, respectively. The uniform manifold approximation and projection (UMAP) analysis identified all of the major cell types in hippocampus based on their unique gene expression signatures (Fig. 3E and fig. S5). No apparent difference in cell type distribution was observed in both groups (Fig. 3F), in line with the normal adult hippocampal neurogenesis in *Kat6a*$^{NEX\text{-}cKO}$ mice (fig. S2F). Given our finding that KAT6A deficiency results in cognitive deficits and CA3 synaptic dysfunction, we paid specific attention to the differentially expressed genes (*q* value <0.05, and $|\log_2 FC| > 0.2$) in the CA3 pyramidal neuron cluster (Fig. 3G). On the basis of the analysis of the transcripts from CA3 cluster of *Kat6a*$^{NEX\text{-}cKO}$ mice and hippocampal RNA-seq of *Kat6a*$^{+/-}$ mice, only one common gene (R-spondin 2, *Rspo2*) was significantly down-regulated in both groups, whereas this gene was not changed in CA1 pyramidal neurons and other cell types (Fig. 3, H to I, and fig. S6, A and B). This suggests that *Rspo2* is a promising candidate gene involved in KAT6A-mediated cognitive functions, although other gene expression changes could also play a role in this process (fig. S6C).

RSPO2, belonging to R-spondin family secreted proteins (RSPO1-4), is an activator of Wnt/β-catenin signaling and is involved in development and cancer (*21*–*23*). It is highly expressed in mouse hippocampus (fig. S6D). Consistent with the sequencing data, *Rspo2* expression level was decreased in hippocampi from both *Kat6a*$^{NEX\text{-}cKO}$ (Fig. 3J and fig. S6E) and *Kat6a*$^{+/-}$ mice (fig. S6F). To further confirm that *Rspo2* down-regulation occurs in CA3 pyramidal neurons, we stereotactically injected adeno-associated viruses (AAVs) expressing Cre–green fluorescent protein (GFP) into hippocampal CA3 of *Kat6a*$^{f/f}$ mice. At 4 weeks after virus injection, hippocampal nuclei were isolated and subsequently sorted to enrich the GFP^{+} nuclei (Fig. 3K). Down-regulation of *Rspo2* in CA3 excitatory neurons upon KAT6A deletion was validated by quantitative reverse transcription polymerase chain reaction (qRT-PCR) assays (Fig. 3L).

To test whether KAT6A directly regulates *Rspo2* transcription, we next performed chromatin immunoprecipitation (ChIP) experiments. Because of the lack of a ChIP-grade antibody against KAT6A, we generated and validated a *Kat6a* knock-in mouse strain with a 3× hemagglutinin (HA) tag fused to its C terminus (KAT6A-HA) (Fig. 4, A and B). *Kat6a*$^{HA/HA}$ mice are viable and healthy, suggesting that the KAT6A-HA fusion protein is functional. Using ChIP-qPCR with an HA antibody, strong enrichment of KAT6A was observed at the promoter region of *Rspo2* in hippocampus (Fig. 4C). Significantly, knockout of *Kat6a* in excitatory neurons decreased enrichment of histone H3 lysine 23 acetylation (H3K23ac), but not H3K9ac or H3K14ac (Fig. 4D), in line with the previous studies that KAT6A and its paralog KAT6B were mainly responsible for H3K23ac (*24*, *25*). Together, these results suggest that KAT6A regulates *Rspo2* transcription by modulating H3K23 acetylation on its promoter.

KAT6A regulates RSPO2-mediated Wnt signaling

RSPO2 is a secreted protein and functions as a Wnt agonist to potentiate Wnt/β-catenin signaling by binding to the leucine-rich repeat-containing G protein–coupled receptors 4/5/6 (LGR4/5/6) (*21*, *26*). This prompted us to examine whether KAT6A modulates Wnt signaling in hippocampal CA3 by influencing *Rspo2* expression. Upon ablation of KAT6A, we observed a significant decrease of active β-catenin in protein lysates from CA3, but not in CA1 or dentate gyrus (Fig. 4E). To further dissect this new genetic pathway, we used human monocyte THP-1 cell lines as a model, which displays high endogenous expression of RSPO2 (*27*). Consistently, knockdown of KAT6A markedly reduced RSPO2 expression (Fig. 4F). It also down-regulated axis inhibition protein 2 (AXIN2) and cyclin D1 (CCND1), two classic Wnt target genes, indicating a decrease in Wnt signaling (Fig. 4F). Conversely, treating THP-1 cells with recombinant RSPO2 protein led to an increase in active β-catenin (Fig. 4G), consistent with a previous study (*27*). While KAT6A down-regulation resulted in a significant decrease in active β-catenin and Wnt target gene (AXIN2 and CCND1) expression, RSPO2 recombinant protein treatment completely reversed these effects (Fig. 4, H to I). These findings demonstrate that RSPO2 is necessary for KAT6A-mediated regulation of Wnt signaling.

RSPO2 is essential for hippocampal CA3 synaptic functions

To further examine the expression and function of RSPO2 in hippocampus, we first performed in situ hybridization and observed that *Rspo2* was preferentially expressed in the CA3 pyramidal neurons with low expression levels in ventral CA1 neurons (Fig. 5A and fig. S7, A to D), consistent with our snRNA-seq results (Fig. 5B). This distinct expression pattern of *Rspo2* in hippocampus suggests a unique role in CA3 pyramidal neurons. To directly test it, we crossed *Rspo2*$^{f/f}$ mice with *NEX*-cre line to generate excitatory neuron–specific *Rspo2* knockout mice (*Rspo2*$^{NEX\text{-}cKO}$). Depletion of *Rspo2* mRNA in hippocampus was verified by qRT-PCR assays (Fig. 5C). *Rspo2*$^{NEX\text{-}cKO}$ mice were viable and appeared grossly normal (fig. S7E). The active β-catenin level in hippocampal CA3 of *Rspo2*$^{NEX\text{-}cKO}$ mice was markedly reduced, whereas the noncanonical Wnt/JNK signaling was normal (Fig. 5D), suggesting that RSPO2 is a bona fide enhancer of Wnt/β-catenin signaling in hippocampus.

We next examined the effect of RSPO2 deficiency on the morphology and function of CA3 pyramidal neurons. Just like *Kat6a*$^{NEX\text{-}cKO}$ mice, spine density at stratum radiatum of CA3 pyramidal neurons was decreased in *Rspo2*$^{NEX\text{-}cKO}$ mice compared to controls (Fig. 5E). Correspondingly, we observed a decreased mEPSC frequency, whereas the amplitude of mEPSC was normal (Fig. 5F). In addition, LTP induced by high-frequency stimulation at A/C fibers

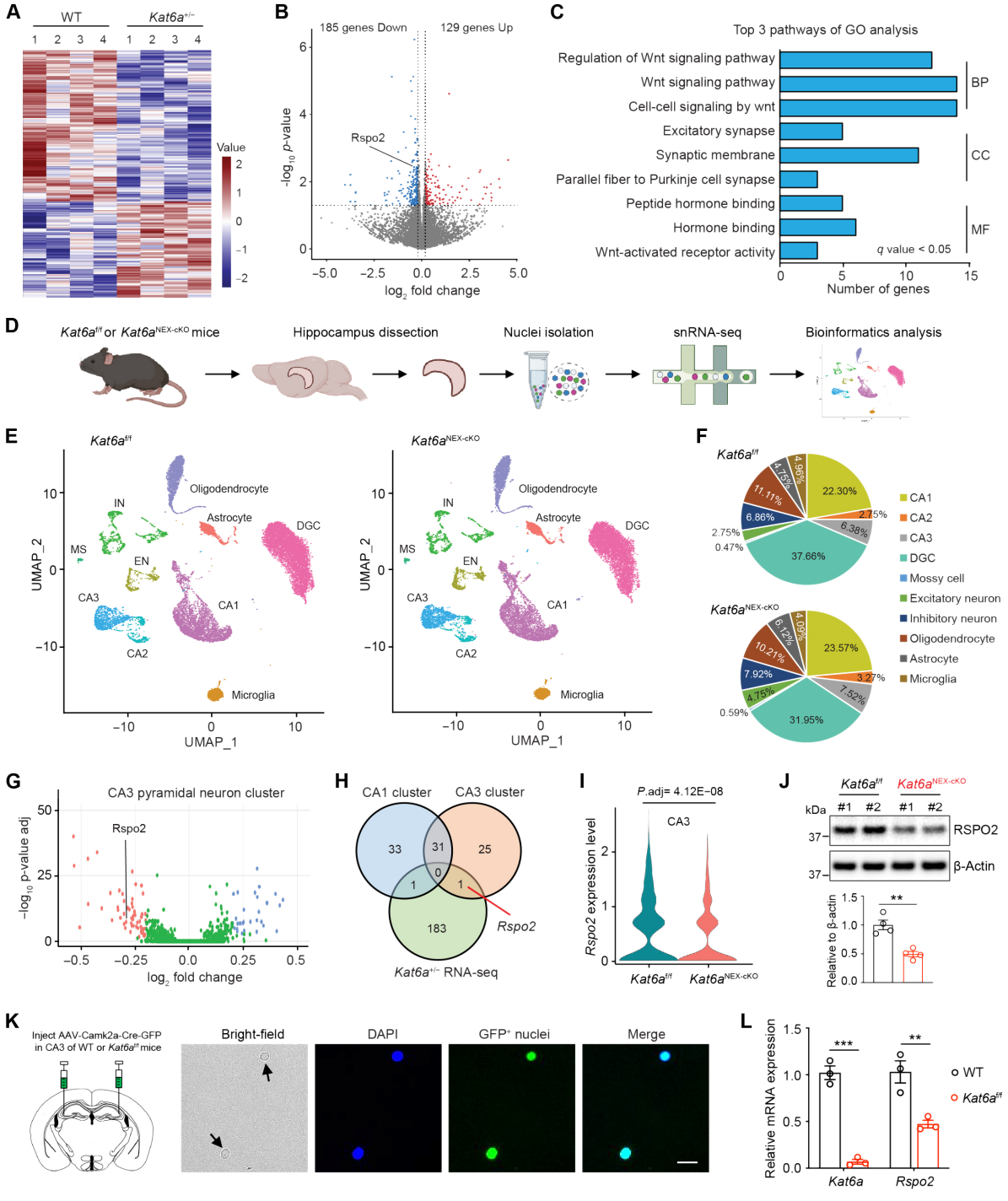

Fig. 3. Identification of *Rspo2* as a key target gene of KAT6A in hippocampal CA3. (**A**) Hippocampus tissues were obtained from adult male WT and *Kat6a*$^{+/-}$ mice, followed by RNA extraction and deep sequencing. Heatmap showing up- or down-regulated genes indicated by red or blue, respectively. (**B**) Volcano plot showing differentially expressed genes (WT versus *Kat6a*$^{+/-}$). (**C**) Classification of the down-regulated genes in *Kat6a*$^{+/-}$ mice with GO analysis. BP, biological process. CC, cellular component. MF, molecular function. (**D**) Flow chart of snRNA-seq using hippocampi from adult male *Kat6a*$^{f/f}$ mice and *Kat6a*$^{NEX\text{-}cKO}$ mice. (**E**) UMAP plot of cell clusters from snRNA-seq. (**F**) Percentile plots of the major hippocampal cell types from snRNA-seq in *Kat6a*$^{f/f}$ mice and *Kat6a*$^{NEX\text{-}cKO}$ mice. (**G**) Volcano plot showing differentially expressed genes in CA3 pyramidal neuron cluster (*Kat6a*$^{f/f}$ versus *Kat6a*$^{NEX\text{-}cKO}$). (**H**) Venn diagram of overlapping down-regulated genes among CA1 pyramidal neuron cluster, CA3 pyramidal neuron cluster, and hippocampal RNA-seq of *Kat6a*$^{+/-}$ mice. (**I**) Violin plot showing expression levels of *Rspo2* in CA3 pyramidal cells from *Kat6a*$^{f/f}$ mice and *Kat6a*$^{NEX\text{-}cKO}$ mice. Unpaired Student's *t* test. (**J**) Western blotting showing deletion of KAT6A decreased RSPO2 expression in hippocampal CA3. Quantification was done by normalizing to β-actin. $n = 4$ mice, unpaired Student's *t* test. (**K**) Scheme (left) of AAV-Camk2a-Cre-GFP virus injection into the mouse hippocampal CA3. Representative images (right) of the GFP$^+$ nuclei from mouse hippocampus after AAV injection. Scale bar, 5 μm. (**L**) qRT-PCR analysis of GFP$^+$ enriched mRNA from WT and *Kat6a*$^{f/f}$ mice for *Kat6a* and *Rspo2*. Two-way ANOVA test. $^{**}P < 0.01$ and $^{***}P < 0.001$. ns, nonsignificant. Data are presented as mean ± SEM.

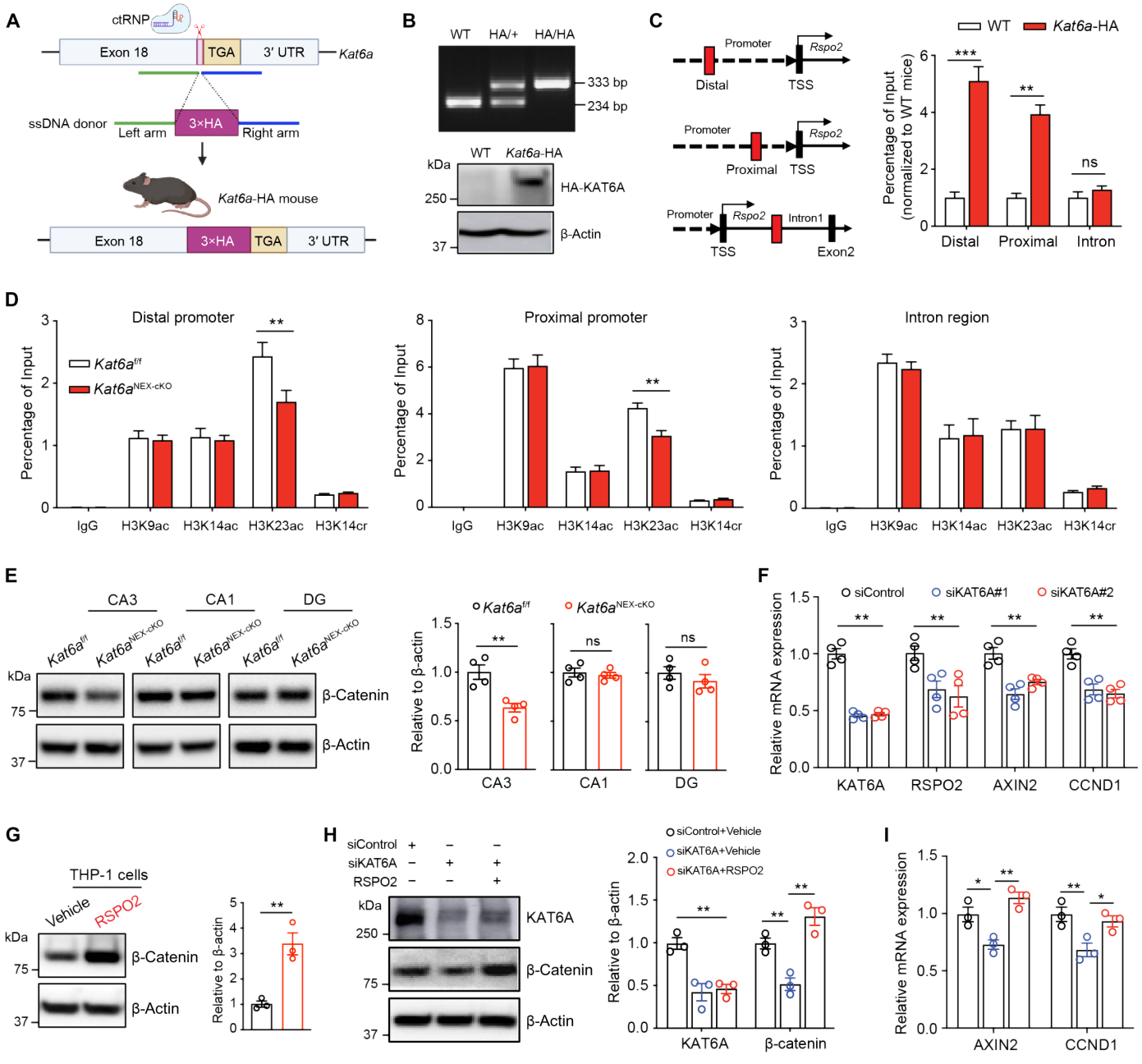

Fig. 4. KAT6A deficiency impairs RSPO2-mediated Wnt signaling. (**A**) Scheme of *Kat6a*-HA mice generation. UTR, untranslated region. (**B**) Validation of *Kat6a*-HA mice by mouse tail genotyping and Western blotting analysis using mouse hippocampal tissues. (**C**) ChIP-qPCR experiments were performed using HA antibody in hippocampus of WT and *Kat6a*-HA mice. Profiles of KAT6A-HA along the mouse *Rspo2* promoter in ~1500 bp (distal) and ~300 bp (proximal) upstream of the transcription start site (TSS). $n = 3$, two-way ANOVA test. (**D**) Deletion of KAT6A resulted in decreased regional enrichment of H3K23ac on the *Rspo2* promoter. Lysates from hippocampal tissues of $Kat6a^{f/f}$ mice and $Kat6a^{NEX\text{-}cKO}$ mice were collected, and ChIP-qPCR assays were performed using the indicated antibodies. $n = 3$, two-way ANOVA test. IgG, immunoglobulin G. (**E**) Western blotting in hippocampal different regions. Quantification was done by normalizing to β-actin. $n = 4$, unpaired Student's t test. (**F**) qRT-PCR analysis showing knockdown of *KAT6A* decreased *RSPO2* and Wnt target genes *AXIN2* and *CCND1* expression in human THP-1 cells. mRNA levels were normalized to *GAPDH*. $n = 4$, two-way ANOVA test. (**G**) Western blotting demonstrating RSPO2 recombinant protein treatment increased active β-catenin expression in human THP-1 cells. Quantification was done by normalizing the level of β-catenin to that of β-actin. $n = 3$, unpaired Student's t test. (**H**) Western blotting showing that RSPO2 incubation could counteract the decrease of active β-catenin induced by knockdown of *KAT6A*. Quantification was done by normalizing the level of β-catenin to that of β-actin. $n = 3$, two-way ANOVA test. (**I**) qRT-PCR analysis showing that RSPO2 incubation reverses the decrease of Wnt target genes *AXIN2* and *CCND1* induced by knockdown of *KAT6A*. mRNA levels were normalized to *GAPDH*. $n = 3$, two-way ANOVA test. $^*P < 0.05$, $^{**}P < 0.01$, and $^{***}P < 0.001$. ns, nonsignificant. Data are presented as mean ± SEM.

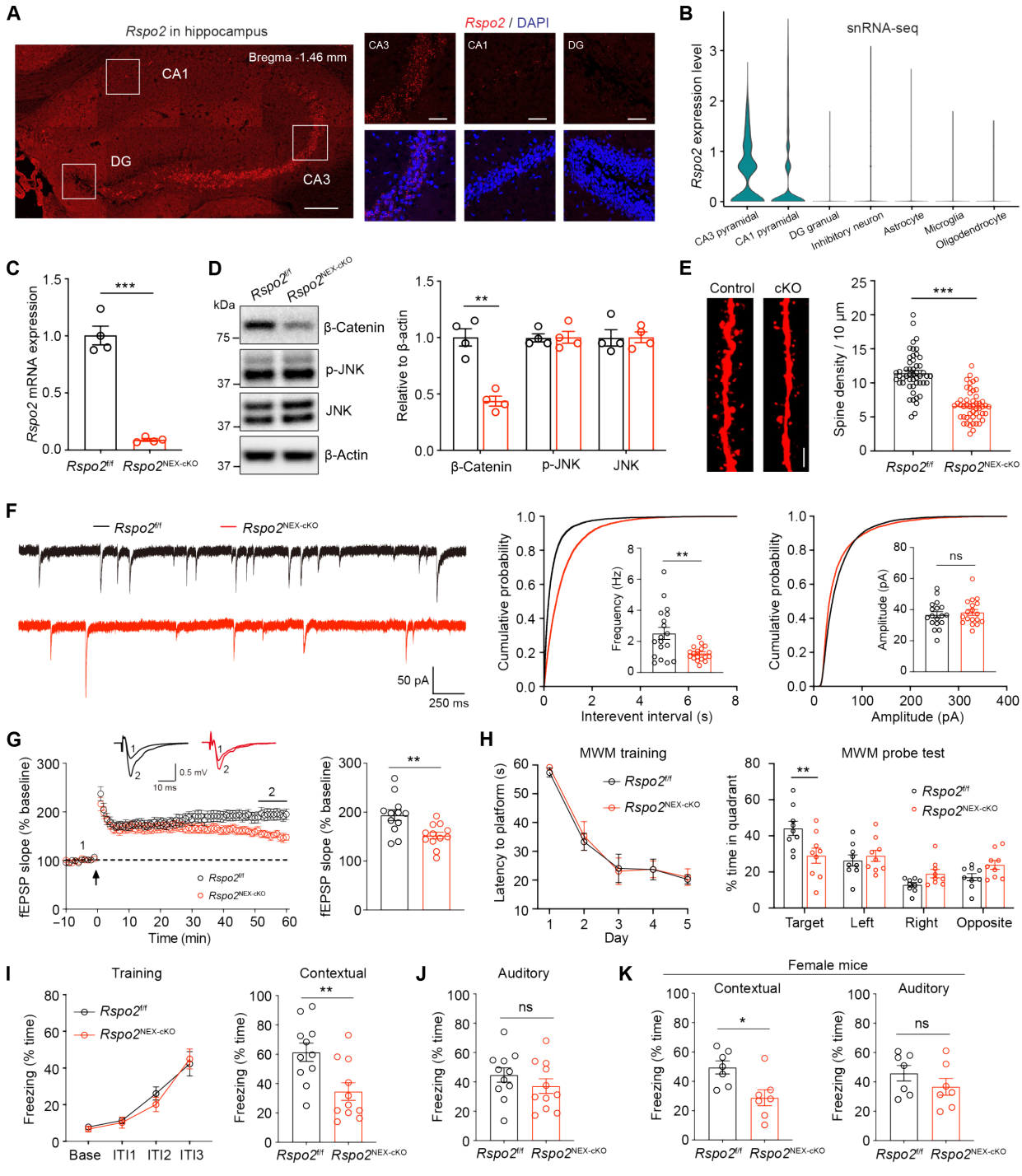

Fig. 5. RSPO2 is essential for hippocampal CA3 synaptic functions. (**A**) Representative images of *Rspo2* RNAscope in situ hybridization in mouse dorsal hippocampus. Scale bars, 200 (left) and 40 μm (right). (**B**) Expression levels of *Rspo2* in hippocampal different cell types from the snRNA-seq of *Kat6a*$^{f/f}$ mice. (**C**) qRT-PCR analysis of total hippocampal mRNA showing that *Rspo2* was deleted in *Rspo2*$^{NEX\text{-}cKO}$ mice. mRNA levels were normalized to *Gapdh*. $n = 4$, unpaired Student's *t* test. (**D**) Western blotting showing that deletion of RSPO2 decreased active β-catenin expression in hippocampal CA3. Quantification was done by normalizing to β-actin. $n = 4$, two-way ANOVA test. (**E**) Left: Representative images of dendritic segments in the stratum radiatum dendrites of CA3 pyramidal neurons. Scale bar, 2 μm. Right: Quantification of dendritic spine numbers. $n = 50$ dendrites from four mice per group. Unpaired Student's *t* test. (**F**) mEPSC in dorsal CA3 pyramidal neurons. $n = 18$ cells from four mice per group. Unpaired Student's *t* test. (**G**) 4× HFS-induced LTP in the presence of DCG-IV at A/C to CA3 synapses. $n = 12$ slices from four mice per group. Unpaired Student's *t* test. (**H**) The MWM test. $n = 9$ mice per group. Two-way ANOVA test. (**I**) Left: Learning curves of male *Rspo2*$^{f/f}$ and *Rspo2*$^{NEX\text{-}cKO}$ mice during the training sessions in fear conditioning test. Two-way ANOVA test. $F(1, 20) = 0.131$, $P = 0.721$. Right: Contextual test in the training context. $n = 11$ mice per group. Unpaired Student's *t* test. (**J**) Auditory test in a novel context. Unpaired Student's *t* test. (**K**) Female *Rspo2*$^{f/f}$ mice and *Rspo2*$^{NEX\text{-}cKO}$ mice were used in fear conditioning test. $n = 7$ mice per group. Unpaired Student's *t* test. $^*P < 0.05$, $^{**}P < 0.01$, and $^{***}P < 0.001$. ns, nonsignificant. Data are presented as mean ± SEM.

to CA3 synapses of *Rspo2*$^{NEX\text{-}cKO}$ mice was also reduced (Fig. 5G). These data suggest that similar to KAT6A, the CA3-enriched RSPO2 is critical for hippocampal CA3 synaptic structure and plasticity.

To explore whether the defective synaptic transmission and plasticity lead to any abnormal animal behaviors, we performed the MWM test to evaluate hippocampus-dependent spatial learning and memory in *Rspo2*$^{NEX\text{-}cKO}$ mice. While they showed a normal learning ability during the training sessions, in the probe test, the mutant mice spent less time in the target quadrant compared to control mice (Fig. 5H). Moreover, the mutant mice displayed decreased context-evoked freezing in the fear conditioning test, with no difference in the tone-evoked freezing behaviors (Fig. 5, I to K), indicating that the memory deficits of *Rspo2*$^{NEX\text{-}cKO}$ mice are hippocampus-dependent. In addition, loss of RSPO2 did not alter the motor abilities or anxiety levels (fig. S7, F and G). Together, these data suggest that RSPO2 deficiency phenocopies the loss of KAT6A, impairing CA3 synaptic functions and disrupting memory formation in hippocampus.

RSPO2 is required for KAT6A-mediated cognitive functions

Given that *Rspo2* is a main transcriptional target of KAT6A in hippocampal CA3 and that RSPO2 depletion impairs memory formation, we hypothesized that RSPO2 is required for KAT6A-dependent synaptic functions. To test this hypothesis, we delivered AAVs expressing either RSPO2-FLAG (AAV-RSPO2) or a control fluorescent protein GFP (AAV-GFP) to the hippocampal CA3 neurons of *Kat6a*$^{NEX\text{-}cKO}$ or control mice by bilateral stereotactic injection (Fig. 6A). At 5 weeks after virus injection, the expression efficiency of RSPO2 protein in CA3 was confirmed by immunostaining (Fig. 6B). Overexpressing the Wnt agonist RSPO2 in the CA3 pyramidal neurons counteracted KAT6A deletion–induced β-catenin decrease in *Kat6a*$^{NEX\text{-}cKO}$ mice (Fig. 6C). Moreover, it enhanced mEPSC frequency and increased the dendritic spine density of these mutant neurons to WT control levels (Fig. 6, D and E, and fig. S8A), indicating that KAT6A-RSPO2 axis is important for hippocampal CA3 synaptic functions.

We further performed a proof-of-concept study to examine whether RSPO2 overexpression ameliorates KAT6A deficiency–induced cognitive defects. Injection of AAV-RSPO2 in the CA3 of *Kat6a*$^{NEX\text{-}cKO}$ mice almost completely rescued the learning and memory deficits in the MWM test (Fig. 6, F to H, and fig. S8B). Furthermore, in the fear conditioning test, while no difference in the tone-evoked freezing was observed in these mice, overexpression of RSPO2 in hippocampal CA3 neurons largely alleviated the context-evoked freezing defects caused by KAT6A deletion (Fig. 6I and fig. S8C). Together, both functional and behavioral data demonstrate that RSPO2 is indispensable for KAT6A-mediated synaptic and cognitive functions and suggest that memory deficits can be reversed in the *Kat6a* mutant mice by elevating canonical Wnt signaling pathway.

DISCUSSION

Our work identifies HAT KAT6A as a critical regulator of hippocampal CA3 synaptic function by modulating RSPO2/Wnt signaling. It reveals the impairment of KAT6A/RSPO2/Wnt signaling pathway as a key molecular mechanism underlying cognitive dysfunction caused by KAT6A deficiency (Fig. 6J). There are currently no treatment options for KAT6A syndrome. Our study suggests that enhancing Wnt signaling in hippocampus is a potential therapeutic strategy for ID, a major clinical feature of this disease.

While HATs can potentially regulate the expression of many genes by altering the chromosome structure, it is interesting that relatively few changes were detected in hippocampus after the loss of *Kat6a*. Only *Rspo2* stood out as a robust transcriptional target of KAT6A. This may reflect functional redundancy between various MYST family proteins, especially its paralog KAT6B. Only acetylation of H3K23 in *Rspo2* promoter region was reduced, while acetylation of other lysine residues was normal. Nevertheless, RSPO2 appears to be the key mediator downstream of KAT6A in hippocampus. First, RSPO2 deficiency phenocopies the loss of *Kat6a*, impairing CA3 synaptic functions and causing memory defects. Second, overexpressing RSPO2 in CA3 pyramidal neurons largely rescues the deficits in both Wnt signaling and memory-related behaviors in *Kat6a* mutant mice. These results support a crucial role of KAT6A-RSPO2 axis in the regulation of synaptic plasticity and hippocampus-dependent memory and underscore the importance of Wnt signaling in the cognitive functions. Notably, *Rspo2* is also highly enriched in basolateral amygdala (BLA) excitatory neurons and functions as a neuronal marker for negative behaviors (*28*). Cre recombinase in *NEX*-cre line was not detected in BLA neurons, suggesting that memory deficits caused by the deletion of KAT6A or RSPO2 in excitatory neurons are unlikely due to the down-regulation of RSPO2 expression in BLA. In addition, osteoblast-specific *Rspo2* knockout mice displayed decreased body size and bone mass (*29*), indicating the growth retardation associated with *Kat6a* haploinsufficiency may be attributable to the reduction of *Rspo2* in the osteoblasts. Together, given the importance of Wnt signaling, KAT6A/RSPO2/Wnt pathway may also play a role in other brain regions or peripheral organs, which are involved in the pathogenesis of KAT6A syndrome.

Hippocampal CA1 region is important for learning and memory, and its neuronal defects are widely implicated in ID-related neurodevelopmental diseases (*30*–*32*). Unexpectedly, loss of KAT6A did not affect CA1 synaptic function. Instead, it impaired CA3 pyramidal neuron synaptic transmission and plasticity, especially those of synapses receiving the prominent recurrent collateral inputs. Consistent with the functional deficits, KAT6A deficiency also decreased dendritic spine density at stratum radiatum layer of CA3 pyramidal neurons, the main region for CA3 recurrent collateral connections. All these defects are dependent on KAT6A-mediated down-regulation of CA3-enriched *Rspo2*, suggesting a unique requirement of strong Wnt signaling for the development and function of CA3 pyramidal neurons. Although Wnt signaling has been involved in regulating synaptic function in other brain regions (*33*, *34*), its molecular mechanism and downstream target genes are still poorly understood. The important role of Wnt signaling in CA3 as we identify here may provide a good model to fill this gap in the future. Together, our work links CA3 dysfunctions and Wnt signaling defects to cognitive deficits associated with KAT6A syndrome, which may also have implications to other ID-related diseases.

MATERIALS AND METHODS

Animals

All procedures related to animal care and treatment were approved by the Johns Hopkins University Animal Care and Use Committee and met the guidelines of the National Institute of Health Guide for the Care and Use of Laboratory Animals. All animals were group housed in a standard 12-hour light/dark cycle with ad libitum access to food and water. Male mice aged 2 to 3 months were used for all

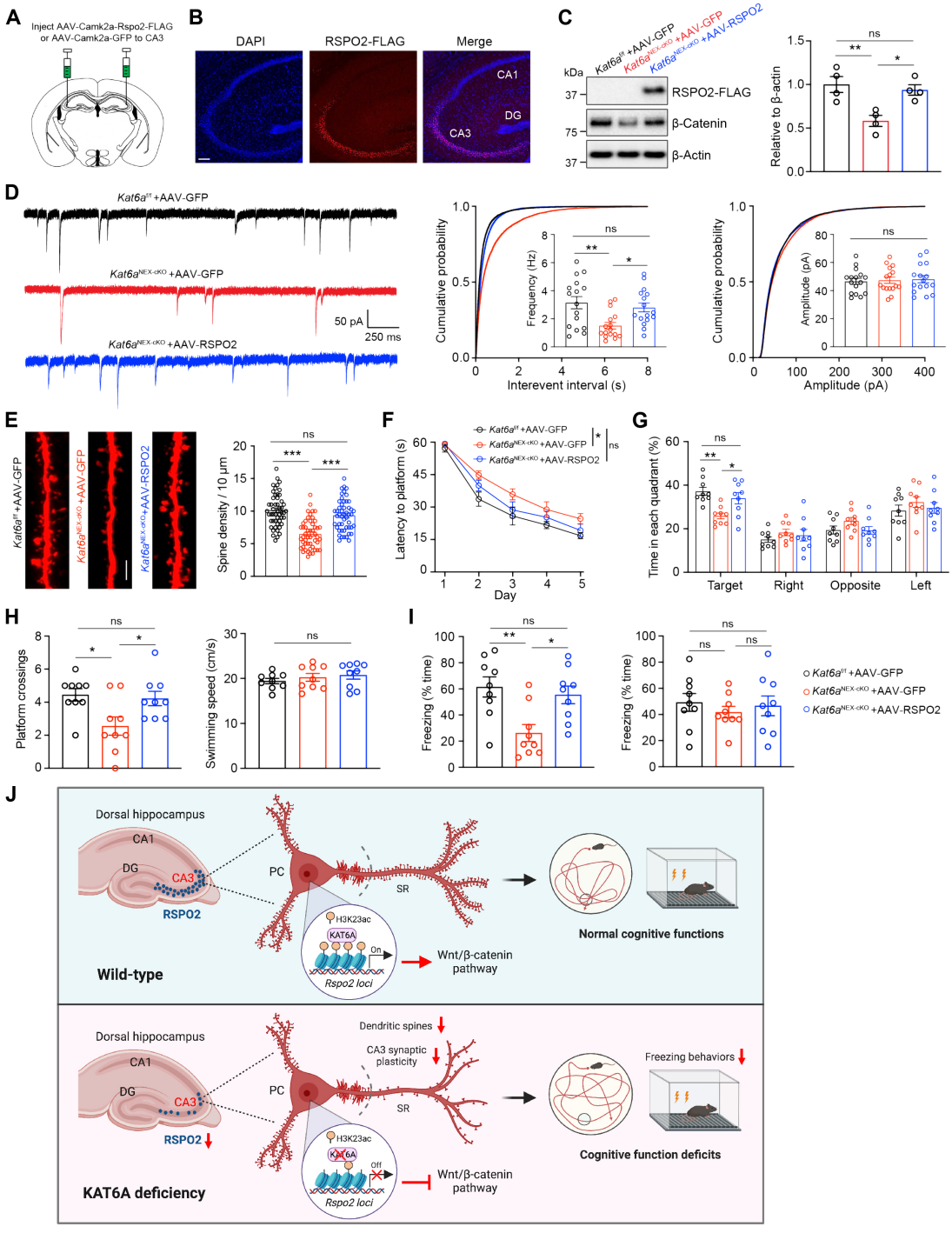

Fig. 6. RSPO2 is required for KAT6A-mediated cognitive functions. (**A**) Scheme of AAV injection. (**B**) Immunofluorescence assays showing the expression of AAV-Camk2a-Rspo2-FLAG viruses in 5 weeks after infecting the mouse CA3 area. Scale bar, 100 μm. (**C**) Western blotting showing that infection of AAV-RSPO2 could counteract the decrease of active β-catenin induced by deletion of KAT6A. Quantification was done by normalizing to β-actin. $n = 4$, one-way ANOVA test. (**D**) Representative traces (left) and quantification of frequency (middle) and amplitude (right) of mEPSC in dorsal CA3 pyramidal neurons of *Kat6a*$^{f/f}$ mice injected with AAV-GFP, *Kat6a*$^{NEX\text{-}cKO}$ mice injected with AAV-GFP, and *Kat6a*$^{NEX\text{-}cKO}$ mice injected with AAV-RSPO2. $n = 16$ cells from four mice per group. One-way ANOVA test. (**E**) Left: Representative *z*-stack images of dendritic segments in the stratum radiatum dendrites of CA3 pyramidal neurons. Scale bar, 2 μm. Right: Quantification of dendritic spine numbers. $n = 50$ dendrites from four mice per group. One-way ANOVA test. (**F**) Time spent before reaching the hidden platform during training days in the MWM test. Two-way ANOVA test. $n = 9$ mice for each group. (**G**) Time spent in different quadrants during the probe test of the MWM test. Two-way ANOVA test. (**H**) Entries into platform zone (left) and swimming speed (right) in the MWM test. One-way ANOVA test. (**I**) Contextual (left) and auditory (right) tests in fear conditioning assays. $n = 9$ mice for each group. One-way ANOVA test. (**J**) Summary diagram showing that the KAT6A-RSPO2 axis is required for memory formation by regulating synaptic structure and plasticity in hippocampal CA3 pyramidal cells (PCs). $^*P < 0.05$, $^{**}P < 0.01$, and $^{***}P < 0.001$. ns, nonsignificant. Data are presented as mean ± SEM.

experiments unless otherwise noted. Female mice were also used for some of the tests. The following mouse lines (8 to 12 weeks old) were used for the experiments: C57BL/6J (Jackson Laboratory, 000664), *Camk2a*-cre (Jackson Laboratory, 005359), *Gfap*-cre (Jackson Laboratory, 024098), *Gad2*-Cre (Jackson Laboratory, 010802), and Ai14 (B6.Cg-Gt(*ROSA*)26*Sor*$^{tm14(CAG-tdTomato)Hze}$/J, Jackson Laboratory, 007914). *NEX*-cre was a gift from N. Klaus-Armin (*35*). *Rspo2* floxed mice were provided from K. Hankenson's laboratory at University of Michigan (*29*). The sequences of the primers used for PCR genotyping are provided in table S2.

Cell culture and siRNA transfection

Human THP-1 cells used were purchased from American Type Culture Collection and maintained in RPMI-1640 medium supplemented with 10% fetal bovine serum and 1% nonessential amino acid at 37°C in humidified 95% CO_2 incubators. Cells were tested negative for mycoplasma contamination before use. siRNAs were purchased from Dharmacon and transfected into THP-1 cells with the final concentration of 30 nM using Lipofectamine RNAiMAX (Invitrogen) according to the manufacturer's instructions. The sequences of siRNA used in this study are as follows: siControl sense, UGGUUUACAUGUCGACUAA; KAT6A siRNA#1 sense, GGAGUUGAGUGUUAAAGAU; siRNA#2 sense, GCGCUAUACUAAUCCAAUA.

Generation of *Kat6a* floxed mice

Kat6a floxed mice were generated at Transgenic Core of Johns Hopkins University using the *Easi*-CRISPR (efficient additions with ssDNA inserts-CRISPR) method, as previously described (*14*). Two single-guide RNAs (sgRNAs) were designed by http://crispor.tefor.net/. The sequences were as follows: sgRNA #1 (reverse strand), ATCTGGGATCTTATCATATCTGG; and sgRNA #2 (forward strand), TTGAGCTGTTTATACTACAGAGG. Two crRNAs containing each sgRNA and ssDNA donor containing the homology arms and the floxed exon sequences were custom synthesized from IDT company. The annealed crRNA and tracrRNA (IDT) were diluted in microinjection buffer (0.25 mM EDTA and 10 mM tris-HCl, pH 7.4) and mixed with Cas9 protein (30 ng/μl; IDT) to obtain ctRNP complexes. One-cell embryos of C57BL/6J mice were microinjected with a mixture of floxing ssDNA donors and two ctRNP complexes and were transferred into the oviducts of pseudopregnant ICR females (Charles River Laboratories). Successful insertions of two LoxP sites were detected by PCR genotyping of mouse tails and confirmed by Sanger sequencing (fig. S1A). During the generation of mice with floxed exons, *Kat6a* knockout mice were also obtained due to the failed homology-directed repair at Cas9 cleavage sites, which were verified by PCR genotyping and Sanger sequencing (fig. S1, B and C). The sequences of the primers used are provided in table S2.

Generation of *Kat6a* 3× HA knockin mice

Kat6a 3× HA knockin mice were generated at Transgenic Core of Johns Hopkins University using the *Easi*-CRISPR method. One sgRNA was designed by http://crispor.tefor.net/. The sequence was as follows: sgRNA (forward strand), CTTACATGAGGAGATGAGCGAGG. One crRNAs containing sgRNA and ssDNA donor containing the homology arms and the 3× HA sequences were custom synthesized from IDT company. The annealed crRNA and tracrRNA (IDT) were diluted in microinjection buffer (0.25 mM EDTA and 10 mM tris-HCl, pH 7.4) and mixed with Cas9 protein (30 ng/μl, IDT) to obtain ctRNP complexes. One-cell embryos of B6SJLF2 mice (Jackson Laboratory) were microinjected with a mixture of ssDNA donors and the ctRNP complexes and were transferred into the oviducts of pseudopregnant ICR females (Charles River Laboratories). Successful insertions of 3× HA were detected by PCR genotyping of mouse tails and confirmed by Sanger sequencing. The sequences of the primers used are provided in table S2.

Real-time qPCR

Total RNA was isolated from samples with TRIzol reagents (Invitrogen) and any potential DNA contamination was removed by RNase-free DNase treatment (Promega, M6101). mRNA was reverse transcribed into cDNA using the high-capacity cDNA reverse transcription kits (Applied Biosystems, no. 4368814). Relative quantitation was determined using the QuantStudio 6 Flex detection system (Applied Biosystems) that measures real-time SYBR green fluorescence and then calculated by means of the comparative Ct method ($2^{-\Delta\Delta Ct}$) with the expression of *Gapdh* as an internal control. The sequences of the primers used are provided in table S3.

Western blot

Proteins were isolated from cultured cells or brain tissues with RIPA buffer (Sigma-Aldrich, R0278) including protease inhibitors cocktails. Samples were resolved on SDS/polyacrylamide gel electrophoresis and transferred to nitrocellulose membranes (Bio-Rad, no. 1620115), which were incubated with appropriate antibodies for overnight at 4°C. Primary antibody concentrations were as follows: anti-HA (rabbit, 1:1000, Cell Signaling Technology, no. 3724), anti–β-actin (mouse, 1:5000, Proteintech, 66009-1-lg), anti-FLAG (mouse, 1:1000, Sigma-Aldrich, F1804), anti-nonphospho (active) β-catenin (rabbit, 1:1000, Cell Signaling Technology, no. 8814), anti-KAT6A (rabbit, 1:1000, Invitrogen, PA5_68046), anti-RSPO2 (rabbit, 1:1000, Biorbyt, orb185986), anti-JNK (rabbit, 1:1000, Cell Signaling Technology, no. 9252), and anti–phospho-JNK (rabbit, 1:1000, Cell Signaling Technology, no. 9251). After wash, the membranes were incubated a horseradish peroxidase (HRP)–conjugated secondary antibody (Cytiva, 1:5000). Immunoreactive bands were visualized using Western Chemiluminescent HRP Substrate (Millipore, no. WBKLS0500) and analyzed with ImageJ [National Institutes of Health (NIH)].

Immunohistochemistry

Anesthetized mice were perfused transcardially with phosphate-buffered saline (PBS), followed by 4% cold paraformaldehyde (PFA) in PBS. Brains were removed and postfixed in 4% PFA at 4°C overnight. After dehydration by 30% sucrose, brains were embedded in OCT (Tissue-Tek) and cut into 30-μm-thick sections on cryostat microtome (Leica). Sections were permeabilized with 0.3% Triton X-100 and 5% bovine serum albumin (BSA) in PBS for 1 hour at room temperature, washed with PBS three times, blocked in 10% BSA, and incubated with primary antibodies at 4°C overnight. Primary antibody concentrations were as follows: anti-FLAG (mouse, 1:100, Sigma-Aldrich, F1804), anti-doublecortin (DCX) (rabbit, 1:100, Cell Signaling Technology, no. 4604), anti-BrdU (mouse, 1:100, Bio-Rad, MCA2483GA), and anti-NeuN (rabbit, 1:200, Cell Signaling Technology, no. 12943). After washing three times with PBS, samples were incubated with Alexa Fluor–conjugated secondary antibodies (1:500, Invitrogen) for 1 to 2 hours at room temperature. Fluorescent images were taken using a confocal microscope (Zeiss LSM 900) and analyzed with ImageJ software (NIH).

ChIP qPCR

ChIP experiments were performed according to the procedure described previously (*36*). Hippocampus tissues from three mice were fixed with 1% formaldehyde for 15 min at room temperature. The fixed cells were lysed in lysis buffer [5 mM EDTA, 50 mM tris-HCl (pH 8.1), and 1% SDS, plus protease inhibitor cocktail]. The lysates were then sonicated with 3 × 10 cycles (30 s on and off) (Bioruptor, Diagenode) to generate chromatin fragments of ~500 bp in length. Cell debris was removed by centrifugation and supernatant were collected. A dilution buffer [2 mM EDTA, 1% Triton X-100, 150 mM NaCl, and 20 mM tris-HCl (pH 8.1), plus protease inhibitor cocktail] was subsequently applied (1:10 ratio) and the resultant chromatin solution (50-μl aliquot as the input) was then incubated with control or specific antibodies (3 to 5 μg) for 12 hours at 4°C with constant rotation. Protein A/G Sepharose beads [50 μl of 50% (v/v)] were added for incubation of another 2 hours. Beads were collected by centrifugation at 500*g* for 5 min at 4°C. Beads were sequentially washed with the following buffers for 5 min at 4°C: TSE I [0.1% SDS, 1% Triton X-100, 2 mM EDTA, 20 mM tris-HCl (pH 8.1), and 150 mM NaCl], TSE II [0.1% SDS, 2 mM EDTA, 1% Triton X-100, 20 mM tris-HCl (pH 8.1), and 500 mM NaCl], buffer III [0.25 M LiCl, 1% Nonidet P-40, 1 mM EDTA, 1% sodium deoxycholate, and 10 mM tris-HCl (pH 8.1)], and tris-EDTA buffer. The input and the precipitated DNA-protein complex were decrosslinked at 65°C for 12 hours in elution buffer [5 mM EDTA, 1% SDS, 50 mM NaCl, 20 mM tris-HCl (pH 8.1), and proteinase K (0.1 mg/ml)], and DNA was purified using PCR purification kit (Qiagen). Quantification of the precipitated DNA fragments were performed with real-time PCR using primers listed in table S4.

RNA sequencing

Four biological replicates were sequenced per group. For each sample, RNA was extracted from hippocampus tissues of littermate controls and *Kat6a*$^{+/-}$ mice, followed by purification with the RNeasy Micro kit (QIAGEN, no. 74004). High-throughput RNA sequencing (RNA-seq) was performed by Illumina NovaSeq 6000 at Novogene (CA, USA). The raw sequencing data were aligned to the mouse preference genome (GRCm38, mm10) using STAR software (v2.5). Reads on each GENCODE annotated gene were counted using HTSeq, and then differential gene expression analysis was performed using DESeq2 R package.

Nuclei isolation

Mouse hippocampal tissues were rapidly dissected in ice-cold homogenization buffer [0.25 M sucrose, 25 mM KCl, 5 mM $MgCl_2$, and 20 mM tricine-KOH, pH 7.8]. The tissue was homogenized using a loose-fitting pestle in 1.5 ml of homogenization buffer supplemented with 1 mM DTT, 0.15 mM spermine, 0.5 mM spermidine, 1× EDTA-free protease inhibitor (Roche), and RNasin Plus RNase Inhibitor (60 U/ml; Promega, N2611). A 6% IGEPAL CA-630 solution was added to bring the homogenate to 0.3% IGEPAL CA-630, and the homogenate was further homogenized with five strokes of a tight-fitting pestle. The sample was filtered through a 50-μm filter (Sysmex, 04-004-2327), underlaid with solutions of 30 and 40% iodixanol (Sigma-Aldrich, D1556) in homogenization buffer, and centrifuged at 10,000*g* for 20 min in a swinging bucket centrifuge at 4°C. Nuclei were collected at the 30 to 40% interface, diluted with two volumes of homogenization buffer, and concentrated by centrifugation for 10 min at 500*g* at 4°C. These nuclei can be used for sorting or snRNA sequencing.

snRNA-seq

Two biological replicates were sequenced per genotype. snRNA-seq libraries were constructed using the 10X Genomics Chromium single cell kit. Libraries were sequenced on an Illumina NovaSeq 6000 at Single Cell and Transcriptomics Core of Johns Hopkins University. Reads were aligned to the mm10 reference genome using the kb-python program (version 0.25.0) (*37*). The data were then imported into R and low-quality nuclei and "empty droplets" were filtered out using the barcodeRanks from the DropletUtils package. The data were analyzed using the Seurat R package (version 4.0.1) as described previously (*38*). In brief, data normalization was performed using SCTransform function. The uwot package (https://github.com/jlmelville/uwot) was used for UMAP dimensional reduction. Seurat FindMarkers function was used for the analysis of differential gene expression and plotted using ggplot2 and the tidyverse collection of R packages in RStudio.

RNAscope in situ hybridization

Fixed brains were embedded in OCT (Tissue-Tek) and sectioned at a thickness of 14 μm. RNAscope Multiplex Fluorescent Reagent Kit v2 (ACD, Advanced Cell Diagnostics) was used following the manufacturer's manual for the fixed frozen tissues. Probe targeting mouse *Rspo2* (no. 402001) was purchased from ACD. TSA Plus fluorescein (no. NEL741E001KT) or cyanine 3 (no. NEL744001KT) was used for developing the fluorescence signal. Images were collected with a Zeiss LSM 900 confocal microscope and analyzed using ImageJ software.

Stereotaxic virus injection

Mice (3 to 6 weeks old) were anesthetized with the inhalation anesthetic isoflurane and positioned in the stereotaxic apparatus (RWD Life Sciences). After craniotomy, the mice were bilaterally injected with 0.5 μl of AAVs into the CA3 (coordinates, bregma: anterior/posterior, −1.8 mm; medial/lateral, ±2.2 mm; and dorsal/ventral: −2.3 mm). After the injection, the needle was maintained in the place for an additional 10 min to facilitate the diffusion of the viruses and then slowly withdrawn. The viruses used in this study were as follows: AAV5-CamkII-GFP-Cre purchased from UNC Vector Core, AAV5-CamkII-GFP purchased from Addgene, and AAV5-CamkII-RSPO2-FLAG packaged from WZ Biosciences Inc. (Maryland, USA). All AAVs were diluted to titers of 3 to 5 × 10^{12} particles per ml. Mice receiving virus injections were returned to their home cages to recover for 4 to 5 weeks before they were used for experiments.

Acute brain slice electrophysiology

For CA1 recordings, hippocampal transverse slices [300 μm for whole-cell recording, while 400 μm for field EPSPs (fEPSP) recording] were cut from 6- to 8-week-old mice using a Leica vibratome in chilled high-sucrose cutting solution containing the following: 2.5 mM KCl, 1 mM NaH_2PO_4, 26 mM $NaHCO_3$, 7 mM glucose, 210 mM sucrose, 0.5 mM $CaCl_2$, and 7 mM $MgSO_4$. Slices were then incubated for 30 min at 34°C in artificial cerebrospinal fluid (aCSF) bubbled with 95% O_2/5% CO_2 containing the following: 119 mM NaCl, 2.5 mM KCl, 26.2 mM $NaHCO_3$, 1 mM NaH_2PO_4, 11 mM glucose, 2.5 mM $CaCl_2$, and 1.3 mM $MgSO_4$. Slices were recovered at room temperature for at least 1 hour. The slices were transferred to a submersion chamber on an upright Olympus microscope and perfused in aCSF containing 0.1 mM picrotoxin and 0.01 mM bicuculline, saturated with 95% O_2/5% CO_2. The perfusion flow rate was maintained constant at 2 ml/min. Recordings were made with MultiClamp 700B

amplifier and 1550B digitizer (Molecular Devices). Data acquisition was performed with pClamp 10.7 software (Molecular Devices), filtered at 2 kHz and digitized at 10 kHz. Whole-cell recordings were made by 3- to 5-megohm borosilicate glass pipettes filled with intracellular solution consisted of the following: 135 mM $CsMeSO_4$, 8 mM NaCl, 10 mM Hepes, 0.3 mM EGTA, 5 mM QX-314, 4 mM Mg–adenosine triphosphate (ATP), 0.3 mM Na–guanosine triphosphate (GTP), and 0.1 spermine. mEPSCs were recorded at a holding potential of −70 mV in the presence of 1 μM tetrodotoxin (TTX). The paired-pulse ratio was measured by applying two pulses at an interval of 25, 50, 100, and 200 ms, respectively, and then calculating the ratio of the peak amplitudes. The input resistance and pipette series resistance were monitored throughout the recording. The fEPSPs were recorded via a glass micropipette filled with ACSF (1 to 3 megohms) placed in the CA1 stratum radiatum. To induce LTP, the stimulation intensity was adjusted to evoke ~30 to 50% of the maximum response. Tris-buffered saline (TBS)–LTP was induced by four trains of theta burst stimulations (five pulses at 100 Hz every 200 ms) with an intertrain interval of 10 s. fEPSP slopes were measured by linear interpolation from 10 to 90% of maximum negative deflection.

For CA3 recordings, 6- to 8-week-old mice were anesthetized with the inhalation anesthetic isoflurane and then perfused intracardially with ice-cold oxygenated cutting solution containing the following: 110 mM choline chloride, 2.5 mM KCl, 1.25 mM NaH_2PO_4, 25 mM $NaHCO_3$, 0.5 mM $CaCl_2$, 7 mM $MgCl_2$, 10 mM glucose, and 3 mM Na-pyruvate, saturated with 95% O_2/5% CO_2. The brain was removed rapidly and immersed in ice-cold oxygenated cutting solution. Transverse hippocampal slices (300 μm for whole-cell recording, while 400 μm for fEPSP recording) were cut in the cutting solution using a vibratome (VT-1200S, Leica) and transferred to aCSF containing the following: 125 mM NaCl, 2.5 mM KCl, 1.25 mM NaH_2PO_4, 25 mM $NaHCO_3$, 2 mM $CaCl_2$, 2 mM $MgCl_2$, 10 mM glucose, and 3 mM Na-pyruvate, saturated with 95% O_2/5% CO_2. The slices were recovered for 30 min at 35°C and then maintained at room temperature for ~1 hour. Slices were subsequently transferred to a submerged recording chamber containing aCSF (without Na-pyruvate) perfusion maintained at 34°C. Recordings were made with MultiClamp 700B amplifier (Molecular Devices). Whole-cell recordings were made by 3- to 5-megohm borosilicate glass pipettes filled with intracellular solution consisted of the following: 120 mM K-gluconate, 15 mM KCl, 10 mM Hepes, 2 mM $MgCl_2$, 0.2 mM EGTA, 4 mM Na_2ATP, 0.3 mM Na_3-GTP, and 14 mM tris-phosphocreatine (pH 7.3). Hippocampal CA3 pyramidal neurons were held at −70 mV and mEPSCs were recorded in the presence of 0.1 mM picrotoxin and 0.5 μM TTX. In the MF blockade experiments, mEPSCs were recorded with 1 μM DCG-IV in the aCSF. Series resistance was monitored throughout each experiment and controlled below 20 megohms. Data were discarded if the series resistance varied more than 20%. For A/C-LTP recordings, a concentric bipolar electrode was placed in CA3 stratum radiatum to stimulate A/C synapses and fEPSPs were recorded with a glass pipette (2 to 3 megohms) filled with aCSF. Picrotoxin (0.1 mM) was added to block inhibitory transmission and 1 μM DCG-IV was added to block MF inputs. The stimulus intensity was adjusted to evoke 40 to 50% of the maximal response. LTP was induced by four trains of 100 Hz (1 s) tetanus with an intertrain interval of 10 s.

Sholl analysis and spine analysis

Recorded pyramidal neurons of CA3 were filled with 0.2% (w/v) biocytin. Then, the slices containing the fixed neurons cross-linked with 4% PFA and stained with streptavidin Alexa Fluor 555 conjugate (Invitrogen, 1:1000). Fluorescent images were obtained using a confocal microscope (ZEISS LSM 900) and imported into ImageJ (NIH) for further analysis. For Sholl analysis, concentric circles at 20-μm intervals were drawn around the soma. The number of dendrites crossing each circle was calculated and the data were presented as mean ± SEM. For spine analysis, dendritic segments at stratum radiatum layer of CA3 were randomly chosen and images were taken with a resolution of 1024 × 1024. An average of three dendrites per neuron on 4 neurons per mouse ($n = 12$ dendrites per mice and $n = 4$ mice per group) totaling ~2000 dendritic spines per experimental group were analyzed. Spines with a neck can be classified as either thin or mushroom, and those without a significant neck are classified as stubby (*39*). Spines with a neck were labeled as thin or mushroom based on head diameter. These parameters have been verified by comparison with trained human operators. The number of dendrites spines is presented as mean ± SEM.

Behavioral tests

Mice were handled by investigators for 4 days before any behavioral test. Mice were given a 2-week interval to recover from the first behavioral test before the next behavioral test. Mice were not subjected to more than three behavioral tests. All behavioral tests were performed at Behavioral Core of Johns Hopkins University.

In the open-field test, mice were placed in a chamber (18″ × 18″) with infrared beams (Photobeam Activity System, San Diego Instruments) and monitored for movement by using horizontal photobeams. Beam breaks were converted to directionally specific movements and summated at 5-min intervals over 15 min. Ambulatory activity (beam breaks) was measured as total horizontal photobeam breaks.

In the elevated plus maze test, we used a plus-shaped platform at 40 cm above the floor with two open arms (30 cm × 5 cm) and two closed arms (30 cm × 5 cm × 15 cm) on opposing sides of a central square platform (5 cm × 5 cm). The overall illuminations of the four arms were kept equal, at 100 to 200 lux. Each animal was gently placed in the center platform facing an open arm and was videotaped for 5 min. The total time and entries in the open arms and the distance the animals traveled were measured using the ANY-maze software. The number of visits to the open arms and the time spent on the open arms were used as measures for anxiety.

For the social interaction test, we used a three-chamber apparatus (60 × 40 × 22 cm) that consisted of three chambers (left, center, and right) of equal size with 10 × 5 cm openings between the chambers. The test consisted of two phases with different stimulus in each of two side chambers. The stimulus was placed inside a capsule (an inverted mesh pencil cup). During habituation, mice were allowed to explore the apparatus with two empty capsules for 10 min. During testing, the first phase contained two identical nonsocial stimuli (paper ball) and the second phase contained a nonsocial stimulus (a Lego cube) and a social stimulus (unfamiliar mouse matched in strain, sex, and age). The test animal was placed in the center of the chamber and allowed to explore the apparatus in the presence of these stimuli for 10 min. Animal behavior during the test session was tracked by a top camera, analyzed by ANY-maze software and verified manually. Interaction time was counted based on close "investigating" behaviors of the test animal to each stimulus. Social preference index = (social time − nonsocial time) / (social time + nonsocial time). The partner mice were used up to three times, with one test per day.

In the NOR test, we used a small chamber (30 cm × 30 cm) to facilitate object exploration and reduce the time needed to habituate mice to the arena. The arena was surrounded on three sides by a white screen to limit spatial information and prevent spatial biases. During the training session, two identical objects (Lego) were placed at left and right sides of the arena. During the training, mice were placed in the center of the arena and allowed to explore freely for 10 min. Mice were returned to their home cages. Then, 2 hours later, one of the objects was replaced by a novel object with different color and shape, and mice were allowed to freely explore the whole arena for 5 min. Animal behavior during the test session was tracked by a top camera, analyzed by ANY-maze software and verified manually. The discrimination index was calculated as (exploration time on the novel object − exploration time on the familiar object) / (exploration time on the novel object + exploration time on the familiar object). Sniffing, touching (>1 s), and staring the objects were judged as exploration behaviors.

In the MWM test, we used a maze consisted of a round pool (diameter, 120 cm) filled with water that was at 24°C and made opaque with nontoxic white tempera paint. A circular plastic platform (diameter, 10 cm) was placed at the center of the target quadrant and submerged 1 cm below the surface of the water. Four local cues were provided to allow spatial map generation. The MWM test was performed as previously described (*40*). In brief, we trained the mice for four trials per day with different start points for five consecutive days. Mice were gently placed into the water facing the wall of the pool and allowed to freely explore the whole maze for 1 min. Mice were then guided to the rescue platform if they did not find it. Mice were allowed to take a rest on the platform for 10 s and then retrained from a different start position with the same procedure. The latency for each animal to find the platform (at least 3-s stay) was recorded. On day 6, the platform was removed, and animals searched freely for 1 min starting from the opposite quadrant. The entries into the platform area, total time spent in the target quadrant, and the total distance travels were recorded using the ANY-maze software. The animals with an average speed below 10 cm/s were excluded for their weak motor ability.

In the fear conditioning test, mice were first habituated to the conditioning chamber (Med Associates Inc.) for 10 min the day before training. On the day of training, after 3-min exploration in the conditioning chamber, each mouse received one pairing of a tone (2800 Hz, 80 dB, 30 s) with a short coterminating foot shock (0.5 mA, 2 s), after which they remained in the chamber for additional 30 s and were then returned to home cages. Twenty-four hours after the conditioning, mice were tested for freezing (behavioral immobility) in response to the training context (training chamber) and to the tone (in the training chamber with a new environment and odor). The percentage of freezing time was calculated as an index of fear learning and memory. For contextual fear memory tests, mice were returned to the conditioning chamber for 3 min and freezing behavior was counted using Video Freeze software (Med Associates Inc.). For auditory fear memory tests, mice were placed in a changed chamber and freezing responses were recorded during the last 3 min when the tone was delivered.

Statistical analysis

Statistical analyses were performed using GraphPad Prism 9.4 (GraphPad Software, La Jolla, CA). Before statistical analysis, variation within each group of data and the assumptions of the tests were checked. For in vivo experiments, the animals were distributed into various treatment groups randomly. For in vitro experiments, the cells were evenly suspended and then randomly distributed in each well tested. Comparisons between two groups were made using unpaired Student's two-tailed *t* test or Mann-Whitney test. Comparisons among three or more groups were made using one- or two-way analysis of variance (ANOVA) followed by Bonferroni's post hoc test. All experiments and analysis of data were performed in a blinded manner by investigators who were unaware of the genotype or manipulation. The significance level was set at $P < 0.05$. Test statistics, *n* numbers, and *P* values are indicated in the figure legends. All data are presented as mean ± SEM.

Supplementary Materials

This PDF file includes:

Figs. S1 to S8
Tables S1 to S4

REFERENCES AND NOTES

1. E. R. Kandel, Y. Dudai, M. R. Mayford, The molecular and systems biology of memory. *Cell* **157**, 163–186 (2014).
2. E. L. Yap, M. E. Greenberg, Activity-regulated transcription: Bridging the gap between neural activity and behavior. *Neuron* **100**, 330–348 (2018).
3. K. K. Lee, J. L. Workman, Histone acetyltransferase complexes: One size doesn't fit all. *Nat. Rev. Mol. Cell Biol.* **8**, 284–295 (2007).
4. J. Humbert, S. Salian, P. Makrythanasis, G. Lemire, J. Rousseau, S. Ehresmann, T. Garcia, R. Alasiri, A. Bottani, S. Hanquinet, E. Beaver, J. Heeley, A. C. M. Smith, S. I. Berger, S. E. Antonarakis, X. J. Yang, J. Cote, P. M. Campeau, De novo KAT5 variants cause a syndrome with recognizable facial dysmorphisms, cerebellar atrophy, sleep disturbance, and epilepsy. *Am. J. Hum. Genet.* **107**, 564–574 (2020).
5. E. Tham, A. Lindstrand, A. Santani, H. Malmgren, A. Nesbitt, H. A. Dubbs, E. H. Zackai, M. J. Parker, F. Millan, K. Rosenbaum, G. N. Wilson, A. Nordgren, Dominant mutations in KAT6A cause intellectual disability with recognizable syndromic features. *Am. J. Hum. Genet.* **96**, 507–513 (2015).
6. K. Yan, J. Rousseau, R. O. Littlejohn, C. Kiss, A. Lehman, J. A. Rosenfeld, C. T. R. Stumpel, A. P. A. Stegmann, L. Robak, F. Scaglia, T. T. M. Nguyen, H. Fu, N. F. Ajeawung, M. V. Camurri, L. Li, A. Gardham, B. Panis, M. Almannai, M. J. G. Sacoto, B. Baskin, C. Ruivenkamp, F. Xia, W. Bi, D. D. D. Study, C. Study, M. T. Cho, T. P. Potjer, G. W. E. Santen, M. J. Parker, N. Canham, M. McKinnon, L. Potocki, J. J. MacKenzie, E. R. Roeder, P. M. Campeau, X. J. Yang, Mutations in the chromatin regulator gene BRPF1 cause syndromic intellectual disability and deficient histone acetylation. *Am. J. Hum. Genet.* **100**, 91–104 (2017).
7. L. Li, M. Ghorbani, M. Weisz-Hubshman, J. Rousseau, I. Thiffault, R. E. Schnur, C. Breen, R. Oegema, M. M. Weiss, Q. Waisfisz, S. Welner, H. Kingston, J. A. Hills, E. M. Boon, L. Basel-Salmon, O. Konen, H. Goldberg-Stern, L. Bazak, S. Tzur, J. Jin, X. Bi, M. Bruccoleri, K. McWalter, M. T. Cho, M. Scarano, G. B. Schaefer, S. S. Brooks, S. S. Hughes, K. L. I. van Gassen, J. M. van Hagen, T. K. Pandita, P. B. Agrawal, P. M. Campeau, X. J. Yang, Lysine acetyltransferase 8 is involved in cerebral development and syndromic intellectual disability. *J. Clin. Invest.* **130**, 1431–1445 (2020).
8. J. Clayton-Smith, J. O'Sullivan, S. Daly, S. Bhaskar, R. Day, B. Anderson, A. K. Voss, T. Thomas, L. G. Biesecker, P. Smith, A. Fryer, K. E. Chandler, B. Kerr, M. Tassabehji, S. A. Lynch, M. Krajewska-Walasek, S. McKee, J. Smith, E. Sweeney, S. Mansour, S. Mohammed, D. Donnai, G. Black, Whole-exome-sequencing identifies mutations in histone acetyltransferase gene KAT6B in individuals with the Say-Barber-Biesecker variant of Ohdo syndrome. *Am. J. Hum. Genet.* **89**, 675–681 (2011).
9. J. Borrow, V. P. Stanton Jr., J. M. Andresen, R. Becher, F. G. Behm, R. S. Chaganti, C. I. Civin, C. Disteche, I. Dube, A. M. Frischauf, D. Horsman, F. Mitelman, S. Volinia, A. E. Watmore, D. E. Housman, The translocation t(8;16)(p11;p13) of acute myeloid leukaemia fuses a putative acetyltransferase to the CREB-binding protein. *Nat. Genet.* **14**, 33–41 (1996).
10. J. B. Baell, D. J. Leaver, S. J. Hermans, G. L. Kelly, M. S. Brennan, N. L. Downer, N. Nguyen, J. Wichmann, H. M. McRae, Y. Yang, B. Cleary, H. R. Lagiakos, S. Mieruszynski, G. Pacini, H. K. Vanyai, M. I. Bergamasco, R. E. May, B. K. Davey, K. J. Morgan, A. J. Sealey, B. Wang, N. Zamudio, S. Wilcox, A. L. Garnham, B. N. Sheikh, B. J. Aubrey, K. Doggett, M. C. Chung, M. de Silva, J. Bentley, P. Pilling, M. Hattarki, O. Dolezal, M. L. Dennis, H. Falk, B. Ren, S. A. Charman, K. L. White, J. Rautela, A. Newbold, E. D. Hawkins, R. W. Johnstone, N. D. Huntington, T. S. Peat, J. K. Heath, A. Strasser, M. W. Parker, G. K. Smyth, I. P. Street, B. J. Monahan, A. K. Voss, T. Thomas, Inhibitors of histone acetyltransferases KAT6A/B induce senescence and arrest tumour growth. *Nature* **560**, 253–257 (2018).

11. B. N. Sheikh, N. L. Downer, B. Phipson, H. K. Vanyai, A. J. Kueh, D. J. McCarthy, G. K. Smyth, T. Thomas, A. K. Voss, MOZ and BMI1 play opposing roles during Hox gene activation in ES cells and in body segment identity specification in vivo. *Proc. Natl. Acad. Sci. U.S.A.* **112**, 5437–5442 (2015).
12. T. Katsumoto, Y. Aikawa, A. Iwama, S. Ueda, H. Ichikawa, T. Ochiya, I. Kitabayashi, MOZ is essential for maintenance of hematopoietic stem cells. *Genes Dev.* **20**, 1321–1330 (2006).
13. J. Kennedy, D. Goudie, E. Blair, K. Chandler, S. Joss, V. McKay, A. Green, R. Armstrong, M. Lees, B. Kamien, B. Hopper, T. Y. Tan, P. Yap, Z. Stark, N. Okamoto, N. Miyake, N. Matsumoto, E. Macnamara, J. L. Murphy, E. McCormick, H. Hakonarson, M. J. Falk, D. Li, P. Blackburn, E. Klee, D. Babovic-Vuksanovic, S. Schelley, L. Hudgins, S. Kant, B. Isidor, B. Cogne, K. Bradbury, M. Williams, C. Patel, H. Heussler, C. Duff-Farrier, P. Lakeman, I. Scurr, U. Kini, M. Elting, M. Reijnders, J. Schuurs-Hoeijmakers, M. Wafik, A. Blomhoff, C. A. L. Ruivenkamp, E. Nibbeling, A. J. M. Dingemans, E. D. Douine, S. F. Nelson, D. D. D. Study, M. Hempel, T. Bierhals, D. Lessel, J. Johannsen, V. A. Arboleda, R. Newbury-Ecob, KAT6A syndrome: Genotype-phenotype correlation in 76 patients with pathogenic KAT6A variants. *Genet. Med.* **21**, 850–860 (2019).
14. H. Miura, R. M. Quadros, C. B. Gurumurthy, M. Ohtsuka, Easi-CRISPR for creating knock-in and conditional knockout mouse models using long ssDNA donors. *Nat. Protoc.* **13**, 195–215 (2018).
15. I. Izquierdo, C. R. Furini, J. C. Myskiw, Fear memory. *Physiol. Rev.* **96**, 695–750 (2016).
16. H. Eichenbaum, Hippocampus: Cognitive processes and neural representations that underlie declarative memory. *Neuron* **44**, 109–120 (2004).
17. T. Nakashiba, J. Z. Young, T. J. McHugh, D. L. Buhl, S. Tonegawa, Transgenic inhibition of synaptic transmission reveals role of CA3 output in hippocampal learning. *Science* **319**, 1260–1264 (2008).
18. K. Nakazawa, M. C. Quirk, R. A. Chitwood, M. Watanabe, M. F. Yeckel, L. D. Sun, A. Kato, C. A. Carr, D. Johnston, M. A. Wilson, S. Tonegawa, Requirement for hippocampal CA3 NMDA receptors in associative memory recall. *Science* **297**, 211–218 (2002).
19. T. A. Macek, D. G. Winder, R. W. T. Gereau, C. O. Ladd, P. J. Conn, Differential involvement of group II and group III mGluRs as autoreceptors at lateral and medial perforant path synapses. *J. Neurophysiol.* **76**, 3798–3806 (1996).
20. H. Kamiya, S. Ozawa, Dual mechanism for presynaptic modulation by axonal metabotropic glutamate receptor at the mouse mossy fibre-CA3 synapse. *J. Physiol.* **518**, 497–506 (1999).
21. O. Kazanskaya, A. Glinka, I. del Barco Barrantes, P. Stannek, C. Niehrs, W. Wu, R-Spondin2 is a secreted activator of Wnt/beta-catenin signaling and is required for Xenopus myogenesis. *Dev. Cell* **7**, 525–534 (2004).
22. S. Seshagiri, E. W. Stawiski, S. Durinck, Z. Modrusan, E. E. Storm, C. B. Conboy, S. Chaudhuri, Y. Guan, V. Janakiraman, B. S. Jaiswal, J. Guillory, C. Ha, G. J. Dijkgraaf, J. Stinson, F. Gnad, M. A. Huntley, J. D. Degenhardt, P. M. Haverty, R. Bourgon, W. Wang, H. Koeppen, R. Gentleman, T. K. Starr, Z. Zhang, D. A. Largaespada, T. D. Wu, F. J. de Sauvage, Recurrent R-spondin fusions in colon cancer. *Nature* **488**, 660–664 (2012).
23. E. Szenker-Ravi, U. Altunoglu, M. Leushacke, C. Bosso-Lefevre, M. Khatoo, H. Thi Tran, T. Naert, R. Noelanders, A. Hajamohideen, C. Beneteau, S. B. de Sousa, B. Karaman, X. Latypova, S. Basaran, E. B. Yucel, T. T. Tan, L. Vlaminck, S. S. Nayak, A. Shukla, K. M. Girisha, C. Le Caignec, N. Soshnikova, Z. O. Uyguner, K. Vleminckx, N. Barker, H. Kayserili, B. Reversade, RSPO2 inhibition of RNF43 and ZNRF3 governs limb development independently of LGR4/5/6. *Nature* **557**, 564–569 (2018).
24. D. Lv, F. Jia, Y. Hou, Y. Sang, A. A. Alvarez, W. Zhang, W. Q. Gao, B. Hu, S. Y. Cheng, J. Ge, Y. Li, H. Feng, Histone acetyltransferase KAT6A upregulates PI3K/AKT signaling through TRIM24 binding. *Cancer Res.* **77**, 6190–6201 (2017).
25. B. J. Klein, S. M. Jang, C. Lachance, W. Mi, J. Lyu, S. Sakuraba, K. Krajewski, W. W. Wang, S. Sidoli, J. Liu, Y. Zhang, X. Wang, B. M. Warfield, A. J. Kueh, A. K. Voss, T. Thomas, B. A. Garcia, W. R. Liu, B. D. Strahl, H. Kono, W. Li, X. Shi, J. Cote, T. G. Kutateladze, Histone H3K23-specific acetylation by MORF is coupled to H3K14 acylation. *Nat. Commun.* **10**, 4724 (2019).
26. H. X. Hao, Y. Xie, Y. Zhang, O. Charlat, E. Oster, M. Avello, H. Lei, C. Mickanin, D. Liu, H. Ruffner, X. Mao, Q. Ma, R. Zamponi, T. Bouwmeester, P. M. Finan, M. W. Kirschner, J. A. Porter, F. C. Serluca, F. Cong, ZNRF3 promotes Wnt receptor turnover in an R-spondin-sensitive manner. *Nature* **485**, 195–200 (2012).
27. R. Sun, L. He, H. Lee, A. Glinka, C. Andresen, D. Hubschmann, I. Jeremias, K. Muller-Decker, C. Pabst, C. Niehrs, RSPO2 inhibits BMP signaling to promote self-renewal in acute myeloid leukemia. *Cell Rep.* **36**, 109559 (2021).
28. J. Kim, M. Pignatelli, S. Xu, S. Itohara, S. Tonegawa, Antagonistic negative and positive neurons of the basolateral amygdala. *Nat. Neurosci.* **19**, 1636–1646 (2016).
29. M. N. Knight, K. Karuppaiah, M. Lowe, S. Mohanty, R. L. Zondervan, S. Bell, J. Ahn, K. D. Hankenson, R-spondin-2 is a Wnt agonist that regulates osteoblast activity and bone mass. *Bone Res.* **6**, 24 (2018).
30. G. L. Caldeira, A. S. Inacio, N. Beltrao, C. A. V. Barreto, M. V. Rodrigues, T. Rondao, R. Macedo, R. P. Gouveia, M. Edfawy, J. Guedes, B. Cruz, S. R. Louros, I. S. Moreira, J. Peca, A. L. Carvalho, Aberrant hippocampal transmission and behavior in mice with a stargazin mutation linked to intellectual disability. *Mol. Psychiatry* **27**, 2457–2469 (2022).
31. A. Pavlowsky, J. Chelly, P. Billuart, Emerging major synaptic signaling pathways involved in intellectual disability. *Mol. Psychiatry* **17**, 682–693 (2012).
32. S. Jawaid, G. J. Kidd, J. Wang, C. Swetlik, R. Dutta, B. D. Trapp, Alterations in CA1 hippocampal synapses in a mouse model of fragile X syndrome. *Glia* **66**, 789–800 (2018).
33. A. Marzo, S. Galli, D. Lopes, F. McLeod, M. Podpolny, M. Segovia-Roldan, L. Ciani, S. Purro, F. Cacucci, A. Gibb, P. C. Salinas, Reversal of synapse degeneration by restoring Wnt signaling in the adult hippocampus. *Curr. Biol.* **26**, 2551–2561 (2016).
34. R. F. Narvaes, C. R. G. Furini, Role of Wnt signaling in synaptic plasticity and memory. *Neurobiol. Learn. Mem.* **187**, 107558 (2022).
35. S. Goebbels, I. Bormuth, U. Bode, O. Hermanson, M. H. Schwab, K. A. Nave, Genetic targeting of principal neurons in neocortex and hippocampus of NEX-Cre mice. *Genesis* **44**, 611–621 (2006).
36. Y. Liu, S. Lai, W. Ma, W. Ke, C. Zhang, S. Liu, Y. Zhang, F. Pei, S. Li, M. Yi, Y. Shu, Y. Shang, J. Liang, Z. Huang, CDYL suppresses epileptogenesis in mice through repression of axonal Nav1.6 sodium channel expression. *Nat. Commun.* **8**, 355 (2017).
37. P. Melsted, A. S. Booeshaghi, L. Liu, F. Gao, L. Lu, K. H. J. Min, E. da Veiga Beltrame, K. E. Hjorleifsson, J. Gehring, L. Pachter, Modular, efficient and constant-memory single-cell RNA-seq preprocessing. *Nat. Biotechnol.* **39**, 813–818 (2021).
38. J. Wang, A. Rattner, J. Nathans, A transcriptome atlas of the mouse iris at single-cell resolution defines cell types and the genomic response to pupil dilation. *eLife* **10**, e73477 (2021).
39. Y. Liu, M. Li, M. Fan, Y. Song, H. Yu, X. Zhi, K. Xiao, S. Lai, J. Zhang, X. Jin, Y. Shang, J. Liang, Z. Huang, Chromodomain Y-like protein-mediated histone crotonylation regulates stress-induced depressive behaviors. *Biol. Psychiatry* **85**, 635–649 (2019).
40. M. Fan, Y. Liu, Y. Shang, Y. Xue, J. Liang, Z. Huang, JADE2 is essential for hippocampal synaptic plasticity and cognitive functions in mice. *Biol. Psychiatry* **92**, 800–814 (2022).

Acknowledgments: We thank K. Hankenson for providing the *Rspo2*-floxed mice, A. Rattner for the technical assistance on snRNA-seq, and J. Nathans, and members of the Qiu lab for valuable discussions. **Funding:** This work was supported by NIH grants R35GM124824, R01NS118014, and RF1NS134549 (to Z.Q.) and RF1NS113820, RF1NS127925, and R01AG078948 (to S.S.). Z.Q. was also supported by McKnight Scholar Award, Klingenstein-Simon Scholar Award, Sloan Research Fellowship in Neuroscience, and Randall Reed Scholar Award. J.Y. was supported by AHA Career Development Award and NARSAD Young Investigator Grant. **Author contributions:** Y.L. initiated the project and performed the majority of the experiments. M.F. and J.Y. performed electrophysiological recordings. L.M., Y.Y., and S.S. analyzed the sequencing data. K.H.C. performed the genotyping of *Rspo2* mice. Y.L., M.F., J.Y., L.M., and Z.Q. analyzed and interpreted the results. Y.L. and Z.Q. designed the study and wrote the paper, with input from all authors. **Competing interests:** The authors declare that they have no competing interests. **Data and materials availability:** RNA-seq data and snRNA-seq data have been deposited in Gene Expression Omnibus (GEO) with accession number of GSE261058 and GSE261148, respectively. All other data needed to evaluate the conclusions in the paper are present in the paper and/or the Supplementary Materials.

Submitted 14 November 2023
Accepted 15 April 2024
Published 17 May 2024
10.1126/sciadv.adm9326